Torque Quality Improvement in Induction Motor for Electric Vehicle Application Based on Teamwork Optimization

Anjan Kumar SAHOO [1], *Ranjan Kumar JENA* [2]

[1]Department of Electrical Engineering, Biju Patnaik University of Technology, Chhend Colony, 769004 Rourkela, India
[2]Department of Electrical Engineering, Centre for Advanced Post Graduate Studies, Biju Patnaik University of Technology, Chhend Colony, 769004 Rourkela, India

anjank.sahoo@gmail.com, ranjankjena@gmail.com

DOI: 10.15598/aeee.v20i4.4538

Article history: Received Nov 13, 2021; Revised Feb 08, 2022; Accepted Apr 03, 2022; Published Dec 31, 2022.

Abstract. *The tailpipe emission caused by the vehicles using internal combustion engines is a significant source of air pollution. To reduce the health hazards caused by air pollution, advanced countries are now adopting the use of Electric Vehicles (EVs). Due to the advancement of electric vehicles, research and development efforts are being made to improve the performance of EV motors. With a nominal reference stator flux, the classical induction motor drive generates significant flux, torque ripple, and current harmonics. In this work, a Teamwork Optimization Algorithm (TOA)-based optimal stator flux strategy is suggested for torque ripple reduction applied in a Classical Direct Torque Controlled Induction Motor (CDTC-IM) drive. The suggested algorithm's responsiveness is investigated under various steady-state and dynamic operating conditions. The proposed Direct Torque Controlled Induction Motor (DTC-IM) drive's simulation results are compared to those of the CDTC-IM and Fuzzy Direct Torque Controlled Induction Motor (FDTC-IM) drives. The proposed system has been evaluated and shown to have reduced torque ripple, flux ripple, current harmonics, and total energy consumption by the motor. Further, a comparative simulation study of the above methods at different standard drive cycles is presented. Experimental verification of the proposed algorithm using OPAL-RT is presented. The results represent the superiority of the proposed algorithm compared to the CDTC- and FDTC-IM drive. The torque ripple reduction approach described in this study can also be applied to all types of induction motors, not only those for electric vehicles or Hybrid Electric Vehicles (HEVs).*

Keywords

Direct torque control, electric vehicle, induction motor, torque ripple.

1. Introduction

The global climate and environment are under severe threat as a result of carbon emissions from internal combustion engine-powered cars. The growing usage of fossil fuels in these cars is a significant contributor to global warming and climate change concerns [1]. According to a recent study, transportation accounts for 24 % of worldwide carbon dioxide emissions. Another research conducted by the European Union indicates that the transport industry accounts for around 27 % of carbon dioxide (CO_2) emissions, with road transport accounting for 70 % of emissions directly [2]. To address these issues, Electric Vehicles (EVs) have garnered widespread interest worldwide because of their zero greenhouse gas emissions, minimal noise, lightweight construction, enhanced performance, and great efficiency [3].

The electrical motor drive is the critical enabler technology for electric and hybrid vehicles. Permanent Magnet Synchronous Motors (PMSM) and Induction Motors (IMs) are the most widely accepted motors for vehicle application due to their high energy and torque densities, higher efficiency, and many other advantages, as presented [4]. An induction

motor is regarded as the best choice for electric vehicle application in the metropolitan driving cycle due to its low cost, less maintenance, good efficiency, and reliability [5]. Induction motor drive control techniques are well-documented in the literature. To achieve fast dynamic response, Direct Torque Control (DTC) and Field-Oriented Control (FOC) are frequently utilized in IM drives. Because of its simplicity, DTC looks to be highly useful for EV applications. It does not require any speed or position encoders and only estimates the flux and torque using the observed voltage and current [4]. It also features a quicker dynamic torque response, a low switching frequency, no current regulator, coordinates transformation, and is insensitive to motor parameters other than stator winding resistance. Despite its advantages, traditional DTC has significant downsides, such as high switching loss and torque ripple because of hysteresis bands and the availability of restricted voltage vectors [4].

Several approaches for reducing torque ripple have been documented in the literature [5], [6], [7], [8], [9], [10], [11] and [12]. In [5], a sliding model-based predictive torque control of an induction motor-driven electric vehicle to reduce ripples and harmonic distortion is presented. A nonlinear switching feedback element is incorporated into the prediction equation to address the model uncertainties, disturbances, and variations in motor characteristics. In [6], a Modified Brain Emotional Controller (MBEC) technique for minimizing torque and flux ripples in sensorless Induction Motor drives is proposed. A biologically inspired intelligent speed controller is used to enhance the system's performance. The speed error is determined by integrating MRAS with SVM to operate sensorless DTC. With the integration of the Sensory cortex into the BEC and the accumulation of other limbic system components, the response becomes fast. The Space Vector Modulation (SVM) approach [7] is another way of reducing ripples. A preview approach is utilized at each cycle to acquire the voltage space vector necessary to precisely adjust for the flux and torque errors. SVM correctly determines switching states for the Voltage Source Inverter (VSI) when a voltage modulator is implemented [8]. As a result, DTC-SVM eliminates the need for hysteresis controllers and switching tables found in CDTC systems. However, it necessitates the online computation of multiple complex equations and is dependent on other machine parameters. While the DTC-SVM technique achieves superior performance with a simpler algorithm, it comes at the cost of increased computation time as compared to conventional DTC [9].

The authors in [10] employ Fuzzy Logic Control (FLC) to enhance the performance of the DTC-IM drive. The fundamental benefit of FLC is that it estimates stator resistance change and reduces the developed torque ripple, resulting in accurate and faster operation, as well as dynamic and robust performance. In [11], an FLC-based DTC for analysing the torque ripple of an induction motor drive is described. To eliminate torque pulsation, it works with a fixed switching frequency. A comparison of the predictive approach, FLC, global minimum torque ripple strategy, CFTC strategy, and duty cycle control with SVPWM-based DTC for torque ripple reduction is presented. A novel fuzzy adaptive speed regulator with a weighting factor tuning technique was proposed to reduce flux and torque ripple produced by inaccuracies in external sensors and an unsuitable weighting factor over a wide speed range [12].

Pulse-Width Modulation (PWM) is incorporated into the DTC to ensure a constant switching frequency. PWM-DTC additionally ensures excitation, reduction of switching losses, and THD minimization for two and multi-level VSIs [13] and [14]. As a result, it is used in both sensored and sensorless IM drives equipped with DTC. The authors in [15] and [16] show a relationship between over-modulation operation and dc-Link voltage fluctuation to reduce the actual torque ripple in the over-modulation area. The over-modulation module's reference voltage amplitude [15] and the period of the voltage space vector [16] are dynamically modified in response to variations in the dc-Link voltage. As a consequence, the torque ripple produced by dc-Link voltage variation is reduced.

The stator flux reference magnitude has a considerable effect on the torque ripples in DTC. The nominal stator flux value is not appropriate for a wide range of load profiles. As a result, the reference flux is optimized in response to the torque to limit torque ripples [17]. However, these methods are based on approximate mathematical relationships between the reference stator flux and torque. In [18], fuzzy logic is used as a stator flux optimizer to select the reference flux value in DTC. The fuzzy membership functions, on the other hand, are asymmetric over the operational range. Self-regulating ANFIS, ANN and FLC are used to optimize the reference flux via torque variations for performance improvement [19]. These soft computing approaches are not widely used in electric vehicle applications due to the high computational costs and complexity of the system. In [20], a stator flux optimizer based on TOA is used for efficiency improvement. However, along with efficiency, there is a significant reduction in ripples, which motivates us to apply the same technique for ripple minimization.

In this paper, a novel torque ripple controller based on optimized stator flux selection is proposed. The TOA is used to estimate the optimized value of the stator reference flux corresponding to the instantaneous speed and torque magnitude. This technique aims for

the improvement in torque ripple at both steady-state and dynamic operating conditions. The usefulness of the suggested method is demonstrated, and the motor's speed response and torque ripple are studied for various vehicle operating modes using simulation and experimental data. The dynamics of the proposed methodology are compared with CDTC and FDTC and presented in this paper through a simulation study. A comprehensive analysis with different standard drive cycles is also presented. The results presented in the paper also represent a reduction in flux ripple, current harmonics, and energy consumption, along with the reduction in torque ripple.

2. Conventional Direct Torque Control (CDTC)

The authors in [21], [22] and [23] discuss the Conventional Direct Torque Control (CDTC) for induction motors. DTC operates on the premise of directly applying a control sequence to the voltage source inverter switches [23]. The sequence is decided with the help of a switching table and two hysteresis regulators; it has the objective of controlling the machine's electromagnetic torque and flux in a decoupled manner. The dynamic characteristics and control algorithm of the induction motor are described here with the help of the following equations as described by [23]. The stator and rotor fluxes are used as state variables in the stator reference frame to describe the following mathematical expressions:

$$\begin{cases} \overline{V}_s = R_s\overline{I}_s + \dfrac{d\overline{\psi}_s}{dt}, \\ 0 = R_r\overline{I}_r + \dfrac{d\overline{\psi}_r}{dt} - j\omega\overline{\psi}_r, \end{cases} \tag{1}$$

$$\begin{cases} \overline{\psi}_s = L_s\overline{I}_s + L_M\overline{I}_r, \\ \overline{\psi}_r = L_r\overline{I}_r + L_M\overline{I}_s. \end{cases} \tag{2}$$

By eliminating $\overline{I}_s$, and $\overline{I}_r$ from Eq. (1) and Eq. (2), the induction machine equation takes the state variable form, which can be represented as:

$$\frac{\mathrm{d}}{\mathrm{d}t}\begin{pmatrix}\overline{\psi_s}\\ \overline{\psi_r}\end{pmatrix} = \begin{pmatrix} -\dfrac{R_s}{\sigma L_s} & \dfrac{R_s L_m}{\sigma L_s L_r} \\ \dfrac{R_r L_m}{\sigma L_s L_r} & \left(j\omega - \dfrac{R_r}{\sigma L_r}\right)\end{pmatrix} \cdot \begin{pmatrix}\overline{\psi_s}\\ \overline{\psi_r}\end{pmatrix} + \begin{pmatrix}1\\0\end{pmatrix}\overline{v_s}, \tag{3}$$

where R_s and R_r are the stator and rotor resistances. L_s, L_r and L_m are self-inductance of the stator, rotor, and mutual inductance between them. ψ_s and ψ_r are stator and rotor flux vectors, respectively. ω is the angular rotor speed measured in electrical radian.

The most appropriate way to design a three-phase machine is by a two-phase model expressed in the (d, q) reference frame, which simplifies the complexity of representing in the (a, b, c) reference frame. Where the state variable can be represented with their d- and q- axis components as $\psi_s = \psi_{\mathrm{ds}} + j\psi_{\mathrm{qs}}$, $\psi_r = \psi_{\mathrm{dr}} + j\psi_{\mathrm{qr}}$ [23].

The electromagnetic torque equations expressed as a function of state variables are given by [23]:

$$\begin{cases} T_{\mathrm{em}} = \dfrac{3pL_m}{2\sigma L_s L_r}\mathrm{Im}\left\{\psi_s \cdot \psi_r^*\right\}, \\ J \cdot \dfrac{\mathrm{d}\Omega}{\mathrm{d}t} + f \cdot \Omega = T_{\mathrm{em}} - T_r. \end{cases} \tag{4}$$

Using Eq. (3), the stator flux can be calculated as shown in Eq. (5) and Eq. (6) [22] in the stationary reference frame as follows:

$$\overline{\psi}_s(t) = \int_0^t \left(\overline{V}_s(t) - R_s\overline{i}_s(t)\right)\mathrm{d}t. \tag{5}$$

From Eq. (3), the stator flux components along the d and q axis are given as:

$$\begin{cases} \psi_{\mathrm{ds}}(t) = \int \left(V_{\mathrm{ds}}(t) - R_s i_{\mathrm{ds}}(t)\right)\mathrm{d}t, \\ \psi_{\mathrm{qs}}(t) = \int \left(V_{\mathrm{qs}}(t) - R_s i_{\mathrm{qs}}(t)\right)\mathrm{d}t. \end{cases} \tag{6}$$

Using Eq. (6), the magnitude and phase angle of the stator flux in the stationary reference frame can then be estimated as:

$$\psi_s = \sqrt{\psi_{\mathrm{ds}}^2 + \psi_{\mathrm{qs}}^2} \quad \text{and} \quad \theta_s = \tan^{-1}\frac{\psi_{\mathrm{qs}}}{\psi_{\mathrm{ds}}}. \tag{7}$$

As per Eq. (6), the stator resistance R_s must be known to estimate electromagnetic torque and stator flux. However, for simplicity neglecting resistance, we can have [23]:

$$\Delta\overline{\psi}_s = \overline{V}_s\Delta t. \tag{8}$$

As per Eq. (8) the application of a stator voltage vector for a small period of time can regulate the stator flux. Hysteresis controllers are used to control the magnitude of the flux by selecting appropriate increments in the voltage vector to keep the flux within the prescribed hysteresis band, as seen in Fig. 1.

A two-level hysteresis comparator is used to regulate the stator flux, while a three-level hysteresis comparator is used to control the electromagnetic torque [23]. The outputs are estimated by the electromagnetic torque and stator flux error, which are called δT_e and $\Delta\Psi_s$, respectively, as indicated in Eq. (9) and Eq. (10). The corresponding hysteresis bandwidths are

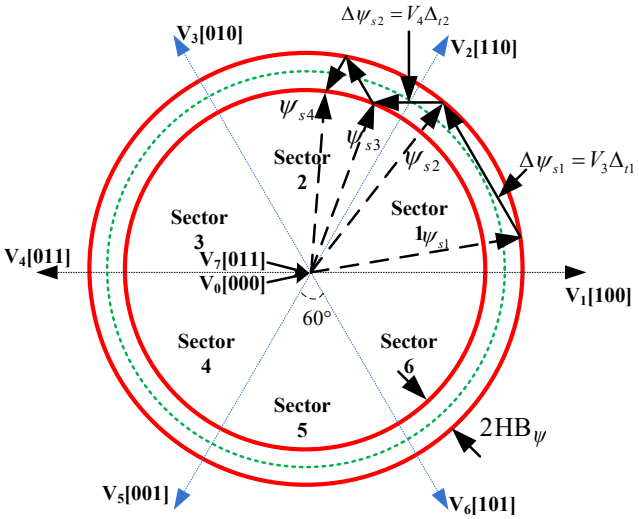

(a) Trajectory of the stator flux vector.

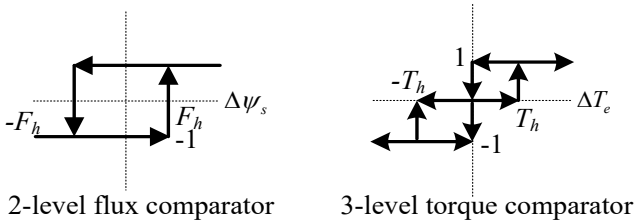

(b) Flux and torque comparator.

Fig. 1: CDTC (a) trajectory of the stator flux vector, (b) flux and torque comparator.

represented by HBT_e and HB_Ψ, respectively:

$$\mathrm{HT}_e = \begin{cases} 1 & \text{for} \quad \Delta T_e > \mathrm{HBT}_e, \\ 0 & \text{for} \quad -\mathrm{HBT}_e < \Delta T_e < \mathrm{HBT}_e, \\ -1 & \text{for} \quad \Delta T_e < -\mathrm{HBT}_e. \end{cases} \tag{9}$$

$$H_\psi = \begin{cases} 1 & \text{for} \quad \Delta\psi_s > \mathrm{HB}_\psi, \\ -1 & \text{for} \quad \Delta\psi_s < -\mathrm{HB}_\psi. \end{cases} \tag{10}$$

Torque and flux are directly regulated in CDTC by selecting a proper voltage vector that causes the stator flux to rotate in response to the desired torque demand depending on the speed error. By comparing the motor's actual and reference speed, the speed error is processed by a PI controller to provide the reference torque output (T^*_{em}). The predicted electromagnetic torque T_{est} and stator flux ψ_{est} are then compared to their corresponding reference values T^*_{em} and ψ^* [23]. The appropriate voltage vector is obtained using the control Tab. 1 based on the flux sector and the outputs of the two hysteresis comparators.

The stator flux reference as expressed in Eq. (11), may be computed using the motor's specifications to ensure that it is sufficient to provide the reference torque:

$$|\psi^*_s| = \sqrt{\frac{4L_s^2 L_r}{3pL_m^2}}. \tag{11}$$

Tab. 1: Stator Voltage vector look-up table.

H_ψ	HT_e	Sector					
		1	2	3	4	5	6
1	1	110	010	011	001	101	100
	0	000	111	000	111	000	111
	−1	110	010	110	010	011	001
−1	1	010	011	001	101	100	110
	0	111	000	111	000	111	000
	−1	001	101	100	110	010	011

3. Proposed Torque Ripple Reduction Algorithm in DTC

In conventional DTC, owing to the inclusion of a hysteresis-band, the switching frequency is variable, which generates current distortion and torque ripples. The purpose of this section is to develop the expression of torque ripple and to evaluate the expression of optimum stator flux to reduce the torque ripple.

3.1. Expression of Torque Ripple

The most distinguishing feature of DTC is its rapid torque response. When the motor is supplied with a suitable voltage vector, the stator flux vector rotates incredibly fast, increasing the angle between the stator and rotor flux. As a result of Eq. (4), the amplitude of the motor torque is increased. If the sampling time Δt is inadequately short, the torque waveform often jumps to the hysteresis band. As a result, the motor torque developed through DTC often exhibits a high torque ripple. This torque ripple has a detrimental impact on the motor's life span and load capacity. Equation (3) is used to compute the stator and rotor fluxes for a small span of time Δt.

$$\begin{cases} \overline{\psi}_{s_{K+1}} = \overline{\psi}_{s_K} + \dfrac{\mathrm{d}\overline{\psi}_{s_K}}{\mathrm{d}t}\Delta t, \\ \overline{\psi}_{r_{K+1}} = \overline{\psi}_{r_K} + \dfrac{\mathrm{d}\overline{\psi}_{r_K}}{\mathrm{d}t}\Delta t. \end{cases} \tag{12}$$

Substituting Eq. (3) in Eq. (12), it can be rewritten as shown in Eq. (13). Rearranging the terms in Eq. (13), it can be expressed as Eq. (14).

Equation (14) expresses the flux of the induction machine in discrete form, valid for a small finite interval. It is worth noting that in Eq. (14), the change in stator flux is due to the applied stator voltage vector for a specific operating state, even though the applied voltage vector is not explicitly mentioned. The stator flux variation is used to illustrate the influence on the rotor flux. Neglecting the effect of stator resistance, Eq. (14) can be rewritten as:

$$\overline{\psi}_{s_{K+1}} = \overline{\psi}_{s_K} + \overline{V}_{s_K}\Delta t. \tag{15}$$

$$\begin{cases} \overline{\psi}_{s_{K+1}} = \overline{\psi}_{s_K} + \left(-R_s \dfrac{\Delta t}{\sigma L_s} \overline{\psi}_{s_K} + \dfrac{R_s L_m}{\sigma L_s L_r} \overline{\psi}_{r_K} + V_{s_K}\right) \Delta t, \\ \overline{\psi}_{r_{K+1}} = \overline{\psi}_{r_K} + \left(\dfrac{R_r L_m}{\sigma L_s L_r} \overline{\psi}_{s_K} + \left(j\omega_K - \dfrac{R_r}{\sigma L_r}\right) \overline{\psi}_{r_K}\right) \Delta t, \end{cases} \tag{13}$$

$$\begin{cases} \overline{\psi}_{s_{K+1}} = \overline{\psi}_{s_K} \left(1 - \dfrac{R_s}{\sigma L_s} \Delta t\right) + \overline{\psi}_{r_K} \left(\dfrac{R_s L_m}{\sigma L_s L_r}\right) \Delta t + \overline{V}_{s_K} \Delta t, \\ \overline{\psi}_{r_{K+1}} = \overline{\psi}_{r_K} \left(1 + \left(j\omega_K - \dfrac{R_r}{\sigma L_r}\right) \Delta t\right) + \overline{\psi}_{s_K} \left(\dfrac{R_r L_m}{\sigma L_s L_r}\right) \Delta t. \end{cases} \tag{14}$$

According to Eq. (15), it seems as if the change in stator flux follows the same direction as the applied voltage, and its magnitude is proportional to the magnitude of, according to Eq. (8). From Eq. (4), the developed motor torque in the $(K+1)^{\text{th}}$ instance can be written as:

$$T_{K+1} = \frac{3pL_m}{2\sigma L_s L_r} \text{Im}\left\{\overline{\psi}_{s_{K+1}} \cdot \overline{\psi}^*_{r_{K+1}}\right\}. \tag{16}$$

Substituting Eq. (14) in Eq. (16) and excluding higher-order terms for simplicity, the torque at $(K+1)^{\text{th}}$ instance can be expressed as:

$$T_{K+1} = T_K - T_K \left(\frac{R_s}{L_s} + \frac{R_r}{L_r}\right) \frac{\Delta t}{\sigma} + \\ + \frac{3pL_m}{2\sigma L_s L_r} \cdot \Delta t \cdot \text{Im}\left\{\overline{V}_{s_K} \overline{\psi}^*_{r_K} - j\omega_K \left[\overline{\psi}_{s_K} \cdot \overline{\psi}^*_{r_K}\right]\right\}. \tag{17}$$

Equation (17) may be rewritten as:

$$\Delta T = T_{K+1} - T_K = \Delta T_{K1} + \Delta T_{K2}, \tag{18}$$

where $\Delta T_{K1} = -T_K \left(\frac{R_s}{L_s} + \frac{R_r}{L_r}\right) \frac{\Delta t}{\sigma}$; $\Delta T_{K2} = K_1 \cdot \Delta t \cdot \text{Im}\left\{\overline{V}_{s_K} \overline{\psi}^*_{r_K} - j\omega_K \left[\overline{\psi}_{s_K} \cdot \overline{\psi}^*_{r_K}\right]\right\}$; and $K_1 = \frac{3pL_m}{2\sigma L_s L_r}$.

The first component is caused by the machine parameters and tends to diminish the torque magnitude. This is independent of the stator voltage and rotor speed in the instantaneous state but depends on the instantaneous torque magnitude. The second component denotes the influence of the applied voltage vector on the variation of torque and is dependent on system parameters such as rotor speed and torque. Equation (18) can be further expanded and simplified as:

$$\Delta T = -T_K \left(\frac{R_s}{L_s} + \frac{R_r}{L_r}\right) \frac{\Delta t}{\sigma} + \frac{3pL_m}{2\sigma L_s L_r} \cdot \Delta t \cdot \\ \cdot \text{Im}\left\{\overline{V}_{s_K} \overline{\psi}^*_{r_K} - j\omega_K \left[\overline{\psi}_{s_K} \cdot \overline{\psi}^*_{r_K}\right]\right\} = \\ = -KT_K \Delta t + \frac{3pL_m}{2\sigma L_s L_r} \cdot \Delta t \cdot \\ \cdot \text{Im}\left\{\overline{V}_{s_K} \overline{\psi}^*_{r_K} - j\omega_K \left[\overline{\psi}_{s_K} \cdot \overline{\psi}^*_{r_K}\right]\right\}, \tag{19}$$

where $K = \frac{1}{\sigma}\left(\frac{R_s}{L_s} + \frac{R_r}{L_r}\right)$.

From Eq. (4), the expression of torque for the k-th instance can be expressed as:

$$T_K = \frac{3pL_m}{2\sigma L_s L_r} \text{Im}\left\{\overline{\psi}_{s_K} \cdot \overline{\psi}^*_{r_K}\right\}. \tag{20}$$

Applying Eq. (20) in Eq. (19), the torque ripple expression can be written as:

$$\Delta T = -K \cdot K_1 \Delta t \cdot \text{Im}\left\{\overline{\psi}_{s_K} \cdot \overline{\psi}^*_{r_K}\right\} + \\ + K_1 \Delta t \cdot \text{Im}\left\{\overline{V}_{s_K} \overline{\psi}^*_{r_K} - j\omega_K \left[\overline{\psi}_{s_K} \cdot \overline{\psi}^*_{r_K}\right]\right\} = \\ = K_1 \Delta t \cdot \text{Im}\left\{\overline{V}_{s_K} \overline{\psi}^*_{r_K} - (K + j\omega_K) \left(\overline{\psi}_{s_K} \cdot \overline{\psi}^*_{r_K}\right)\right\}. \tag{21}$$

Using Eq. (1) and Eq. (2), under the steady-state condition, the relation between stator flux and rotor flux can be expressed as:

$$\psi_s = \frac{L_s R_r - j\left(L_m^2 - L_s L_r\right)(\omega - \omega_s)}{L_m R_r} \psi_r = \\ = (a + jb)\psi_r, \tag{22}$$

where:

$$\begin{cases} a = \dfrac{L_s}{L_m}, \\ b = \dfrac{\left(L_m^2 - L_s L_r\right)(\omega - \omega_s)}{L_m R_r}. \end{cases} \tag{23}$$

Using Eq. (22) in Eq. (21) the torque ripple expression as a function of rotor flux, speed and stator voltage can be formulated as:

$$\Delta T = K_1 \Delta t \cdot \text{Im}\left\{V_s \psi^*_r - (K + j\omega)(a + jb)\left(\psi_s \cdot \psi^*_r\right)\right\} \tag{24}$$

After further simplification and considering only the imaginary part, Eq. (24) can further be expanded as:

$$\Delta T = K_1 \Delta t \cdot \left\{\left(V_{\text{qs}} \psi_{\text{dr}} - V_{\text{ds}} \psi_{\text{qr}}\right) - \\ + (a\omega + bK)\left(\psi^2_{\text{dr}} + \psi^2_{\text{qr}}\right)\right\}. \tag{25}$$

If the reference frame is aligned on the rotor flux axis, then the torque ripple in the motor can be calculated

as:

$$\begin{aligned}\Delta T &= K_1 \Delta t \cdot \left\{ V_{\mathrm{qs}} \psi_{\mathrm{dr}} - (a\omega + bK) \psi_{\mathrm{dr}}^2 \right\} = \\ &= K_1 \Delta t \cdot \left\{ V_{\mathrm{qs}} \psi_{\mathrm{dr}} - \right. \\ &\left. + \left(\frac{\omega L_s}{L_m} + \frac{K \left(L_m^2 - L_s L_r \right) (\omega - \omega_s)}{L_m R_r} \right) \psi_{\mathrm{dr}}^2 \right\}. \end{aligned} \tag{26}$$

3.2. TOA-Based Optimal Stator Flux Selection

1) Description of TOA

Population-based optimization algorithms are popular techniques for tackling optimization issues. The algorithm's primary objective is to imitate team members' collaborative behaviors to accomplish a goal. The TOA is theoretically described to ensure that it can solve optimization issues, as presented in [24]. The method is a population-based optimization algorithm built on simulations of team members' interactions and behaviors while completing their jobs and accomplishing the team's intended objective. Thus, search agents are regarded as team members in the TOA, and links between team members serve as a mechanism of transfer of information. The team's objective is to solve the optimization issue.

The TOA updates the algorithm population in three steps.

Stage 1: Supervisor guidance.

This stage involves updating team members as per the instructions of the supervisor. At this point, the supervisor communicates with the members and steers them toward the goal. Equation (27) is used to model this update stage in the TOA:

$$\begin{cases} X_i^{S1} : x_{i,d}^{S1} = x_{i,d} + r \left(s_d - I \cdot x_{i,d} \right), \\ X_i = \begin{cases} X_i^{S1}, & F_i^{S1} < F_i, \\ X_i, & \text{else}, \end{cases} \\ I = \mathrm{round}(1 + r), \end{cases} \tag{27}$$

where F_i^{S1} is the value of the objective function, X_i^{S1} represents the updated weight of d-th problem variable as recommended by an i-th team member following supervisor guidance, r is a random number between $[0, 1]$, and I is the update index.

Stage 2: Information sharing.

Here, each member of the team competes to enhance their performance by utilizing the information from other teammates who have performed better than them. The team members of the proposed TOA are updated based on Eq. (28) and Eq. (29):

$$X^{M,i} : x_d^{M,i} = \frac{\sum_{j=1}^{N_i} x_{j,d}^{g,i}}{N_i}, \tag{28}$$

$$\begin{cases} X_i^{S2} : x_{i,d}^{S2} = x_{i,d} + r \left(x_d^{M,i} - I \cdot x_{i,d} \right) \cdot \\ \cdot \mathrm{sign} \left(F_i - F^{M,i} \right), \\ X_i = \begin{cases} X_i^{S2}, & F_i^{S2} < F_i, \\ X_i, & \text{else}, \end{cases} \end{cases} \tag{29}$$

where $F^{M,i}$ and $F_i{}^{S2}$ are the values of the objective functions, $X^{M,i}$ is the team's average having higher than that of the i-th team member, N_i is the number of members who outperform compared to an i-th teammate, $x_{j,d}^{g,i}$ is the value of the d-th variable recommended by the j-th better team member for the i-th teammate, $X_i{}^{S2}$ is the second stage updated status of an i-th teammate.

Stage 3: Individual activity.

Each member endeavors to enhance their performance based on the present position in this stage. Equation (30) represents the update of teammates for this stage:

$$\begin{cases} X_i^{S3} : x_{i,d}^{S3} = x_{i,d} + (-0.01 + 0.02r)\, x_{i,d}, \\ X_i = \begin{cases} X_i^{S3}, & F_i^{S3} < F_i, \\ X_i, & \text{else}, \end{cases} \end{cases} \tag{30}$$

where $F_i{}^{S3}$ is the value of the objective function, and $X_i{}^{S3}$ is the final status of an i-th team member. The population is updated in three stages for each iteration of the algorithm according to Eq. (27), Eq. (28), Eq. (29) and Eq. (30). The iterative process is repeated until the algorithm reaches the stop criteria. Finally, the TOA provides the optimal solution to the optimization problem.

2) Implementation of TOA for Optimal Flux Selection

In this work, TOA is used to calculate the optimum stator flux for minimizing the torque ripple while satisfying the system constraints. Figure 2 depicts the architecture of the DTC-based IM drive for EV with the recommended loss minimization technique.

- *Objective Function*
  From an induction motor point of view, reduction in the torque ripple is one of the prime objectives for selecting the reference stator flux, as, over time, this torque ripple reduction will be reflected in the

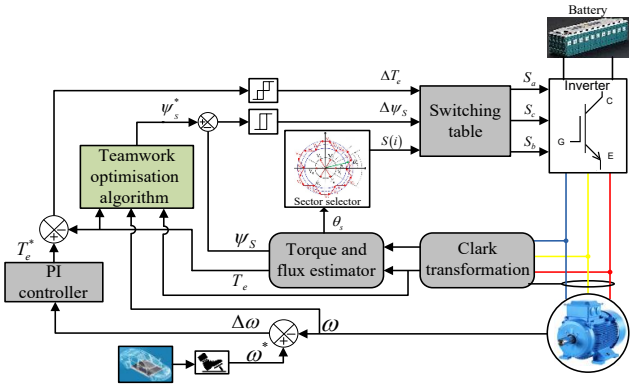

Fig. 2: Block diagram of the proposed DTC for EVs.

stator current THD and energy consumption from the battery. The induction motor torque ripple can be expressed as formulated in Eq. (26).

$$\Delta T = T_{\text{ripple}} = \frac{3pL_m}{2\sigma L_s L_r} \cdot \Delta t \cdot \left\{ V_{\text{qs}} \psi_{\text{dr}} - \right.$$
$$\left. + \left(\frac{\omega L_s}{L_m} + \frac{K\left(L_m^2 - L_s L_r\right)(\omega - \omega_s)}{L_m R_r} \right) \psi_{\text{dr}}^2 \right\}. \tag{31}$$

So, the objective function can now be formulated using Eq. (26):

$$f = \min(T_{\text{ripple}}). \tag{32}$$

- *Constraints*
  The objective function described in Eq. (32) is optimized using TOA for the following pragmatic constraints.
  - *d*-axis rotor flux: The *d*-axis rotor flux is allowed to vary within the minimum and maximum permissible rotor flux:

$$\psi_{\text{dr}}^{\min} \leq \psi_{\text{dr}} \leq \psi_{\text{dr}}^{\max}. \tag{33}$$

- *Generation of the initial population*
  In the present work, TOA is used to compute the optimal *d*-axis rotor flux to minimize the power loss of the induction machine. The initial population of the TOA contains the uniformly distributed *d*-axis rotor flux values as specified by Eq. (34):

$$X_i = \psi_{\text{dr}}^{\min} + \text{rand} \cdot \left(\psi_{\text{dr}}^{\max} - \psi_{\text{dr}}^{\min}\right). \tag{34}$$

- *Detail steps of Implementation*
  The detailed implementation steps of the proposed algorithm to minimize the power loss of the induction machine are described in the flow chart as shown in Fig. 3.

However, as stator flux control is required for a DTC-based IM drive, a simple conversion between stator and

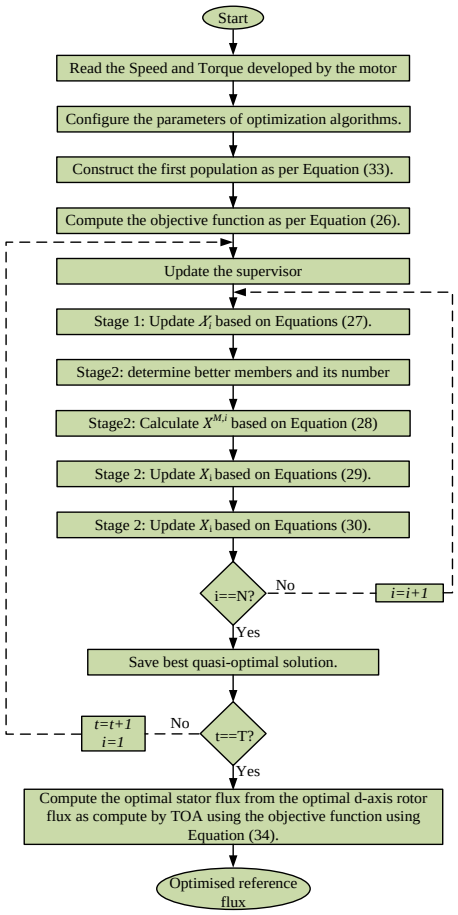

Fig. 3: Flowchart of the proposed TOA.

rotor fluxes may be employed. As a consequence, the optimal reference value for stator flux is as follows:

$$\psi_s^* = \psi_s^{\text{ref}} = \frac{L_s}{L_m} \sqrt{\left(\psi_{\text{dr}}^*\right)^2 + \left(\frac{2}{3}\frac{\sigma L_r}{p}\right)^2 \left(\frac{T_e^{\text{ref}}}{\psi_{\text{dr}}^*}\right)^2}. \tag{35}$$

4. Results and Discussion

To evaluate the effectiveness of the suggested TOA-based stator flux Optimized DTC (ODTC), a simulation-based comparison among Classical DTC (CDTC) [23], Fuzzy DTC (FDTC) [10], and proposed ODTC is presented here. Table 2 depicts the specifications of the induction motor utilized in the simulation study. The simulations are conducted in MATLAB/Simulink environment with a simulation step time of 25 µs.

Simulation studies are conducted for all three methodologies under consideration. A speed profile with starting, constant speed, acceleration, and breaking, a profile comparable to that used in electric vehicle

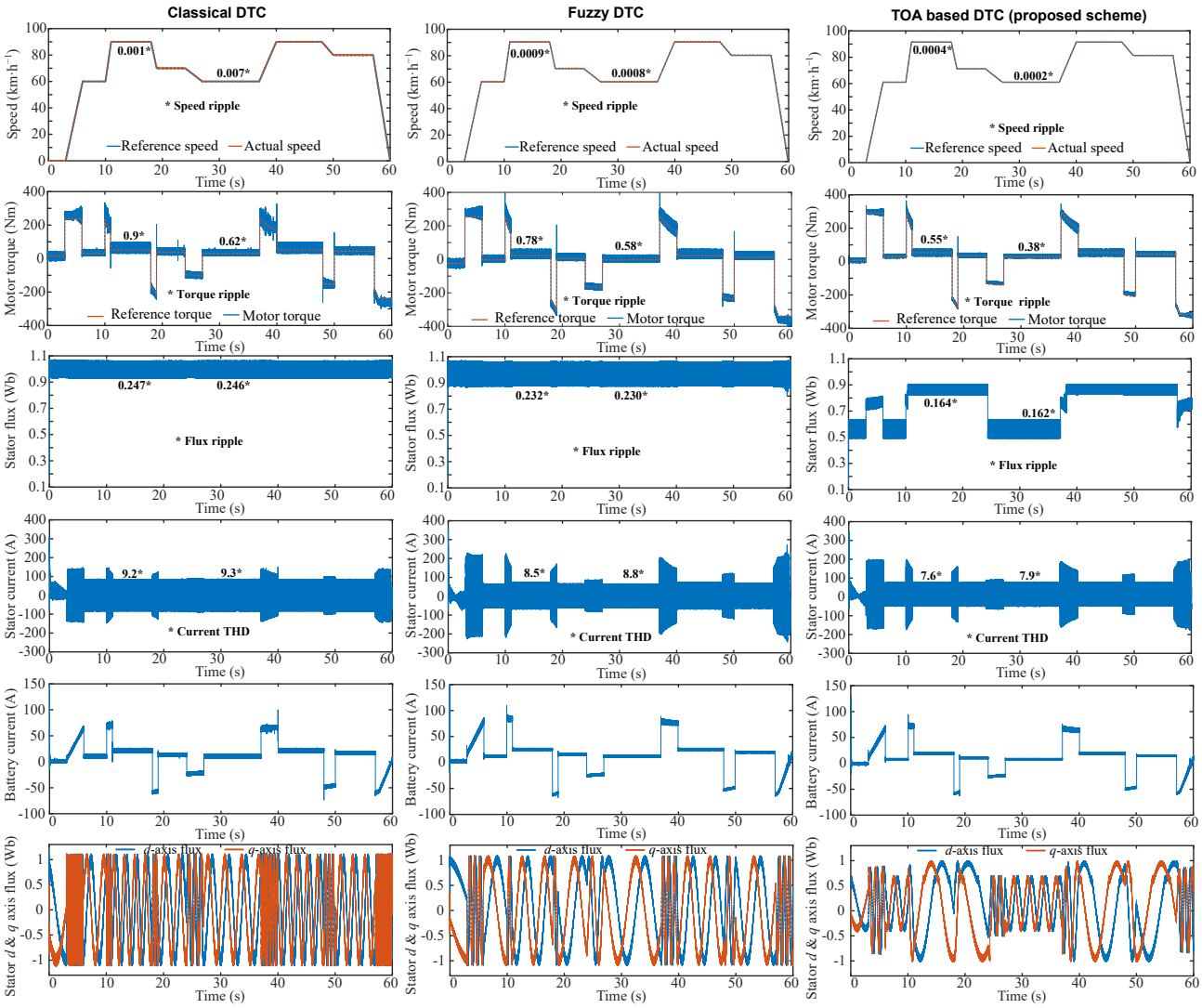

(a) CDTC. (b) FDTC. (c) ODTC.

Fig. 4: Performance of the electric vehicle with (a) CDTC, (b) FDTC, and (c) ODTC methods.

Tab. 2: IM Parameter.

$\boldsymbol{P}$:	50 hp (37 kW)	$\boldsymbol{L_s = L_r'}$:	$0.724 \cdot 10^{-3}$ H
$\boldsymbol{V}$:	400 V	$\boldsymbol{L_m}$:	$27.11 \cdot 10^{-3}$ H
$\boldsymbol{R_s}$:	$82.33 \cdot 10^{-3}$ Ω	$\boldsymbol{f}$:	50 Hz
$\boldsymbol{R_r'}$:	$50.3 \cdot 10^{-3}$ Ω	$\boldsymbol{p}$:	2

applications, is applied, as shown in Fig. 4. Initially, the vehicle starts and is allowed to build the flux, and in 3 seconds, the speed increases from rest to 60 km·h^{-1}. It continues to run at different speeds and finally comes to rest at 60 seconds. As seen in Fig. 4, the motor can operate reliably under a variety of operating scenarios, which initially validates the suggested method's efficacy.

To demonstrate the advantages of the proposed optimized flux-based DTC of IM for the electric vehicle application and also for a close comparison, the algorithm is compared with the conventional DTC [23] and fuzzy DTC [10], as shown in Fig. 4(a) and Fig. 4(b), respectively. Along with the speed response, Fig. 4 depicts the IM's torque, stator flux, and stator current response. The battery current profile and d-axis q-axis stator flux profile have also been depicted in this figure.

As can be seen, the motor's torque response closely matches the reference value; however, the resulting motor torque in ODTC has the lowest torque ripple among all. There is a reduction of 38.89 % torque ripple in ODTC compared to CDTC, whereas this is 34.48 % with FDTC. Similarly, the reduction in stator current THD is 17.39 % and 10.58 % when compared with CDTC and FDTC, respectively. This reduction in torque ripple and THD is due to the optimal selection of stator flux, which can be observed in Fig. 4. For CDTC and FDTC, the reference flux is constant as

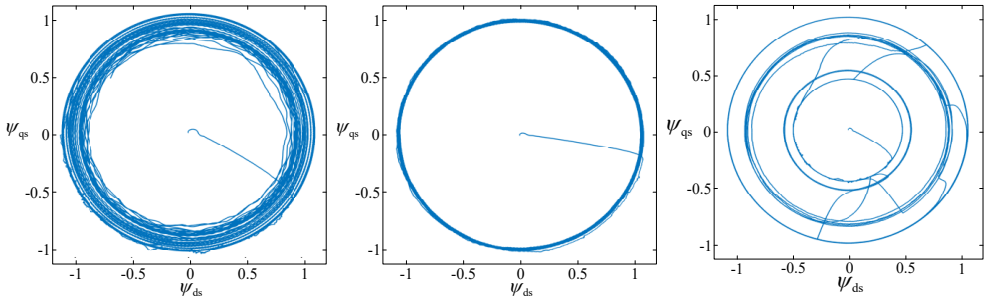

Fig. 5: Flux trajectory for (a) CDTC, (b) FDTC, and (c) ODTC methods.

decided from Eq. (11); however, the reference flux in ODTC is a variable one with speed and load as per Eq. (35). Figure 4 also represents the battery current profile, which shows a rise in current drawn with load and charging of the battery during braking due to regenerative power.

Figure 5 shows the *d-q* trajectory obtained in the stationary reference frame using the three DTC approaches during the driving cycle to demonstrate the substantial reduction in the flux. As presented in Fig. 5, the circular trajectory of the stator flux illustrates the flux trajectory in a DTC drive, whereas Fig. 5(c) demonstrates a dynamic flux magnitude that corresponds to the operating condition, validating the suggested technique.

Figure 6 compares the speed error and battery energy for the three controllers. One can see that the speed error is the minimum in ODTC among all. Due to the reduction in torque ripple and current THD, the battery energy required to drive the vehicle over the entire cycle is also minimum. There is a reduction of 36.2 % and 11.8 % of total battery energy in ODTC compared to CDTC and FDTC, respectively.

Figure 7 and Fig. 8 compare the speed and torque response of all the controllers. As shown in Fig. 7, though the speed response of all three controllers is similar, the proposed technique has a low overshoot and settling time compared to the other two. Similarly, Fig. 8 compares the torque created for the controllers for the entire speed range considering all the controllers. The graph illustrates a considerable reduction in torque ripple for the proposed strategy.

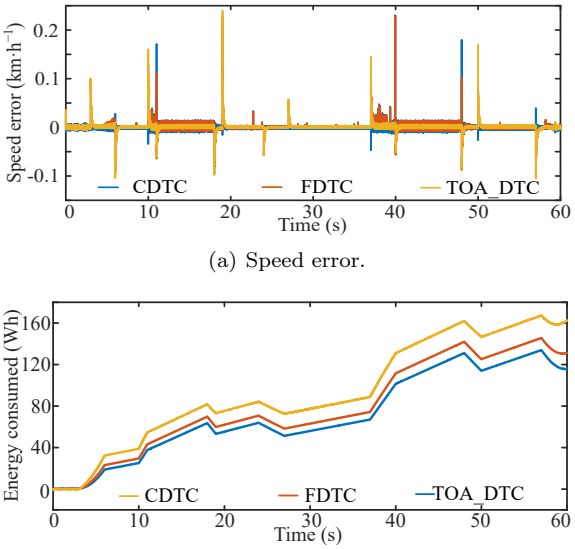

(a) Speed error.

(b) Battery energy.

Fig. 6: Comparison of (a) speed error and (b) battery energy.

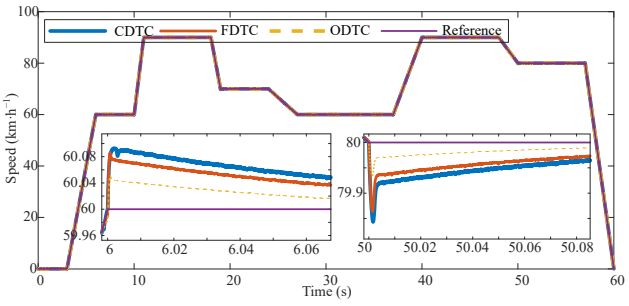

Fig. 7: Comparison of speed response of CDTC, FDTC, and ODTC.

4.1. Steady-State Performance

To demonstrate the proposed ODTC's improved steady-state performance, a complete comparison of CDTC, FDTC, and ODTC is performed under various operating situations, evaluating flux ripple, torque ripple, and current THD. Equation (36) and Eq. (37) are used to determine the flux ripple and torque ripple, respectively:

$$T_{e\_r} = \sqrt{\frac{1}{m}\sum_{j=1}^{m}\left(T_{e\_j} - T_{e\_\mathrm{av}}\right)^2}, \qquad (36)$$

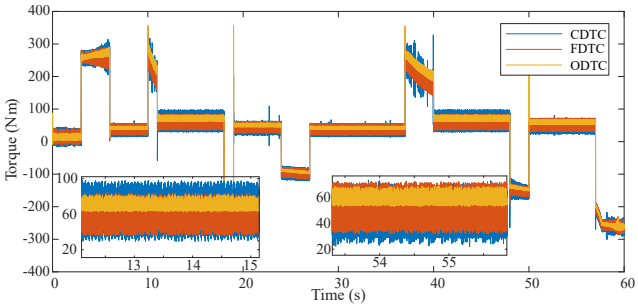

Fig. 8: Comparison of torque response of CDTC, FDTC, and ODTC.

$$\psi_{s\_r} = \sqrt{\frac{1}{m}\sum_{j=1}^{m}\left(\psi_{s\_j} - \psi_{s\_\mathrm{av}}\right)^2}, \qquad (37)$$

where T_{e_j} and ψ_{s_j} are the instantaneous value of the torque and flux; T_{e_av} and ψ_{s_av} are the torque and flux references, respectively.

Figure 9 plots the low-speed operation results of CDTC, FDTC, and ODTC at 20 km·h^{-1}. To provide a clear picture of the performance of the three approaches, the current harmonic spectrums are provided together with the torque, flux, and stator current associated with this speed, from which the current THDs of CDTC, FDTC, and ODTC are found to be 9.3 %, 7.9 %, and 7.3 %, respectively. As a result, we can infer that ODTC has the lowest current total harmonic distortion and the least distorted current waveform at low speeds. It can be noticed that torque ripple is also the minimum among all for ODTC, which is 59.31 % and 49.72 % less compared to CDTC and FDTC, respectively.

Figure 10 provides the results of CDTC, FDTC, and ODTC at a high speed of 80 km·h^{-1}. The current harmonic spectra are presented, with the current THDs of the three approaches being 9.1 %, 7.5 %, and 6.5 %, respectively. As a result, we may continue to see that ODTC has the lowest current THD at high speed. Similarly, the torque ripple for the ODTC method is minimum for high speed also, which is 28.42 % and 20.37 % lesser than CDTC and FDTC, respectively.

As stated above, the quality of flux and torque control has a direct effect on the current THD of the motor drive. Table 3 presents the details of the ripples for torque, flux, and speed as well as current THD at both low and high speeds. Figure 11 depicts the improvement in performance characteristics relative to CDTC and FDTC.

To demonstrate the performance at different operating points, the torque ripple, speed ripple, flux ripple, and stator current THD values of the three approaches were obtained at different speeds and loads and compared in Fig. 12. In Fig. 12, ODTC has a lower flux ripple (0.178 Wb) at 40 km·h^{-1} than CDTC (0.25 Wb) and FDTC (0.241 Wb) at all load conditions. Additionally, ODTC has the lowest torque ripple of 2.7 Nm, 17.14 % less than CDTC and 7 % less than FDTC. Also, the corresponding value of torque ripple in ODTC has the minimum value among all methods. With ODTC, the stator current THD is significantly reduced compared to the other two for the entire range of load as shown in Fig. 12. Analysis at high speed, i.e., at 80 km·h^{-1} and 100 km·h^{-1}, demonstrates that the suggested technique outperforms all other methods in terms of torque ripple across all load ranges, though the flux ripples of all the three approaches are close to each other, ODTC having the minimum value. As a result, it can be concluded that the proposed ODTC has superior steady-state performance over CDTC and FDTC in terms of flux and torque ripples, as well as improved harmonics at low and high speeds. Though the speed ripple in all operating conditions with all three methods is very small, there still exists some improvement in the speed ripple with the proposed one compared to the other two.

4.2. Dynamic Performance

To evaluate the suggested approach's dynamic performance, the results of a simulation study comparing CDTC, FDTC, and ODTC with acceleration, braking, and speed reversal are depicted in Fig. 13, Fig. 14 and Fig. 15.

The vehicle's starting process may be separated into two stages, pre-excitation and acceleration, as seen in Fig. 13. The speed reference is 0 km·h^{-1} during pre-excitation, but the flux reference is its nominal value (1 Wb for CDTC and FDTC, whereas only 0.6 Wb for ODTC). After the switching transient dies out and the stator flux amplitude arrives at its reference value, the reference speed steadily rises to 60 km·h^{-1}, indicating that the operation has entered the acceleration phase. Additionally, as seen in Fig. 13, the flux magnitude increases to 0.8 Wb as the torque developed by the motor increases during this acceleration process. When the motor accelerates, the real-time torques of CDTC, FDTC, and ODTC increase substantially to 150 Nm. Additionally, the time required for the three techniques to achieve the reference speed is almost the same, around 2 ms, indicating that CDTC, FDTC, and ODTC all exhibit a comparable dynamic reaction during the acceleration process.

Figure 14 describes the braking of the vehicle with CDTC, FDTC, and ODTC. Initially, the speed of the vehicle was 60 km·h^{-1}; with the application of the brake, it was reduced to 20 km·h^{-1}. The torque developed by the motor at both the steady-state speeds is low, whereas during braking, the motor develops

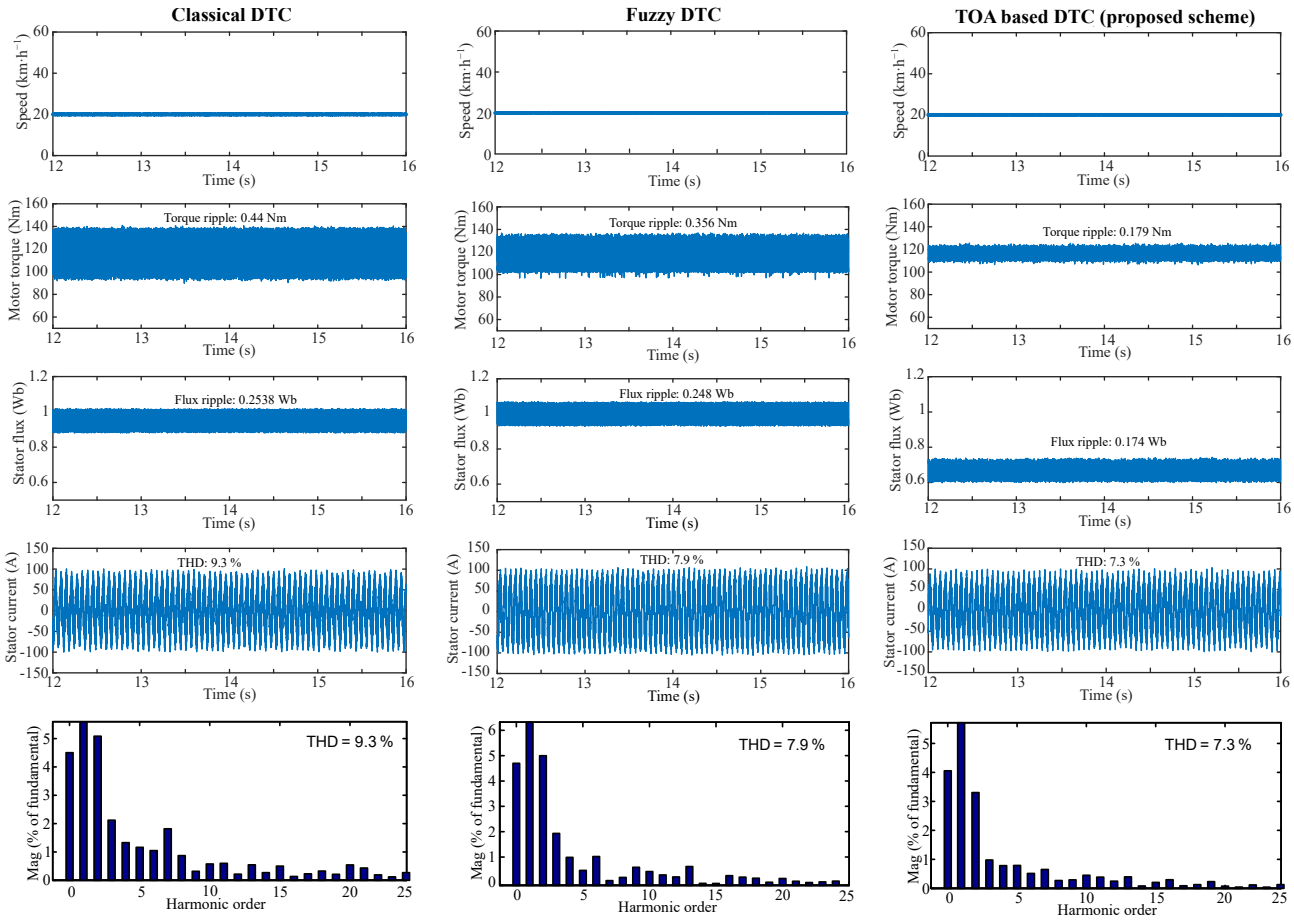

(a) CDTC. (b) FDTC. (c) ODTC.

Fig. 9: Steady-state performance at low speed for (a) CDTC, (b) FDTC, and (c) ODTC methods.

Tab. 3: Performance during steady-state.

Performance	Characteristics	Speed	CDTC	FDTC	ODTC	Improvement (%) w.r.t	
						CDTC	FDTC
Torque	Ripples (Nm)	20 km·h^{-1}	0.44	0.356	0.179	**59.32**	**49.72**
		80 km·h^{-1}	1.48	0.458	0.3506	**76.31**	**23.45**
Flux	Ripples (Wb)	20 km·h^{-1}	0.254	0.248	0.174	**31.5**	**29.84**
		80 km·h^{-1}	0.2403	0.216	0.194	**19.27**	**10.18**
Speed	Ripples (r·min^{-1})	20 km·h^{-1}	0.005	0.0004	0.0002	**96**	**50**
		80 km·h^{-1}	0.006	0.0009	0.0001	**98**	**88.88**
Current	THD (%)	20 km·h^{-1}	9.3	7.9	7.3	**21.5**	**7.6**
		80 km·h^{-1}	9.1	7.5	6.9	**24.17**	**8**

a large negative torque, i.e., around −150 Nm, in this case, to bring the speed down more quickly. In CDTC and FDTC, the flux during the process remains the same, whereas, in ODTC, the flux has increased during braking, which helps the motor to develop the necessary flux more quickly.

As seen in Fig. 15, the vehicle was running with an initial speed of 80 km·h^{-1}, at $t = 25$ seconds gradually the speed starts reducing, and finally, at $t = 30$ seconds, the speed becomes 40 km·h^{-1} but in the opposite direction. Under steady-state, only a small torque is sufficient to drive the vehicle. When the speed reversal is started, it takes almost the same time to arrive at −40 km·h^{-1} by CDTC, FDTC, and ODTC, this shows that the three methods all have the same dynamic response. As described in the braking condition, here also for speed reversal, the motor torque becomes high, so as the stator flux in ODTC, whereas in the other two methods, the flux remains the same. In ODTC, it took only 2 ms to produce the higher value of the

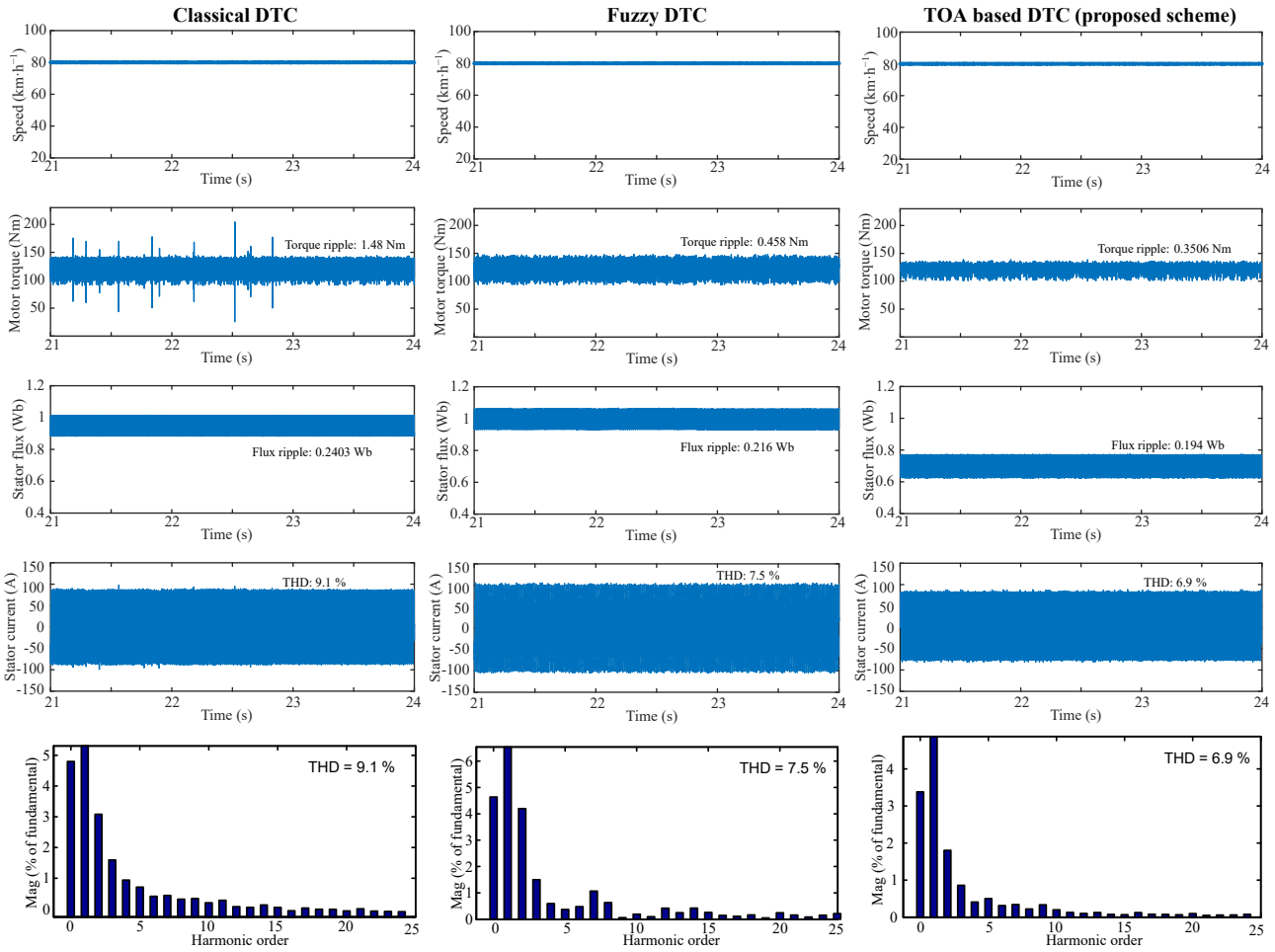

(a) CDTC. (b) FDTC. (c) ODTC.

Fig. 10: Steady-state performance at high speed for (a) CDTC, (b) FDTC, and (c) ODTC methods.

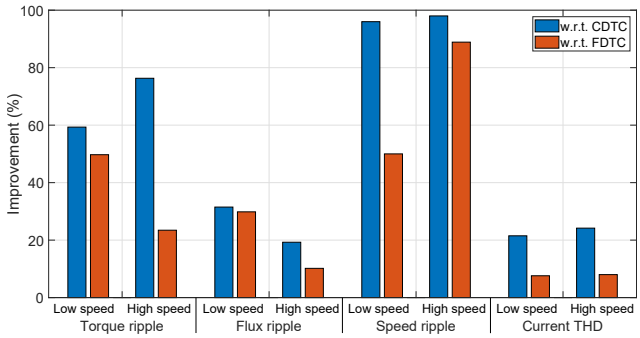

Fig. 11: performance improvement of ODTC at steady-state.

torque with the inception of reversal, whereas this is around 5 ms for CDTC and FDTC.

It can be observed from Fig. 13, Fig. 14 and Fig. 15 that the flux ripple, torque ripple, and current distortion is significantly large with the CDTC method. To evaluate the performance during transient, the Integral Square Error (ISE) of the torque during starting, braking, and speed reversal is computed and displayed in Tab. 4 for all the controllers. Figure 17 displays the torque ISE improvements of ODTC over CDTC and FDTC.

Tab. 4: ISE of the controllers during Transient.

	Starting	**Braking**	**Speed reversal**
CDTC	$6.48 \cdot 10^7$	$4.97 \cdot 10^7$	$9.48 \cdot 10^7$
FDTC	$5.81 \cdot 10^7$	$4.35 \cdot 10^7$	$8.96 \cdot 10^7$
ODTC	$3.41 \cdot 10^7$	$3.02 \cdot 10^7$	$5.84 \cdot 10^7$

4.3. Performance with Standard Drive Cycle

In addition to the above performance, the CDTC, FDTC, and ODTC are also tested considering EUDC and HWFET cycles. The simulated results obtained are shown in Fig. 16 and Fig. 18, respectively. From the figure, it is clear that the vehicle speed tracks the reference speed. With the proposed method, the torque ripple performance is far better superior to CDTC and

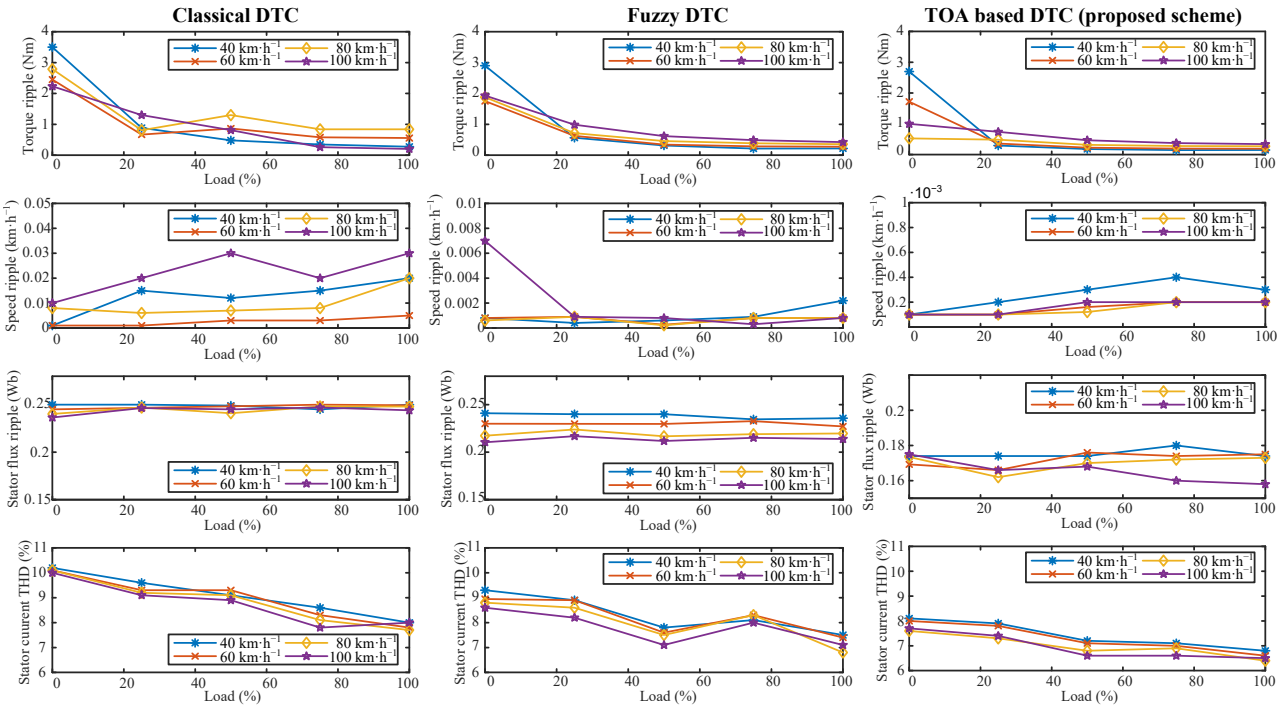

(a) CDTC. (b) FDTC. (c) ODTC.

Fig. 12: Simulation study: induction motor drive characteristics (electromagnetic torque, speed, stator flux, and stator current THD) under the steady-state condition with (a) CDTC, (b) FDTC, and (c) ODTC methods.

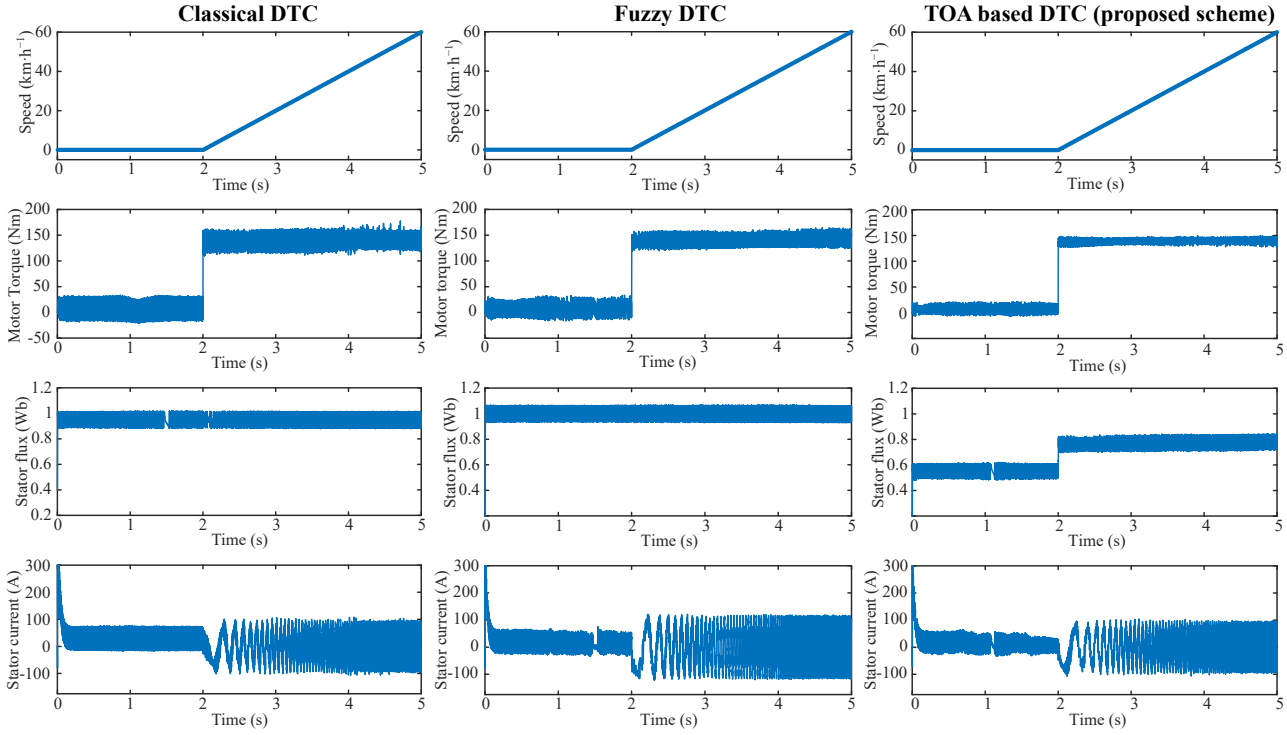

(a) CDTC. (b) FDTC. (c) ODTC.

Fig. 13: Starting response from zero speed to high speed for (a) CDTC, (b) FDTC, and (c) ODTC methods.

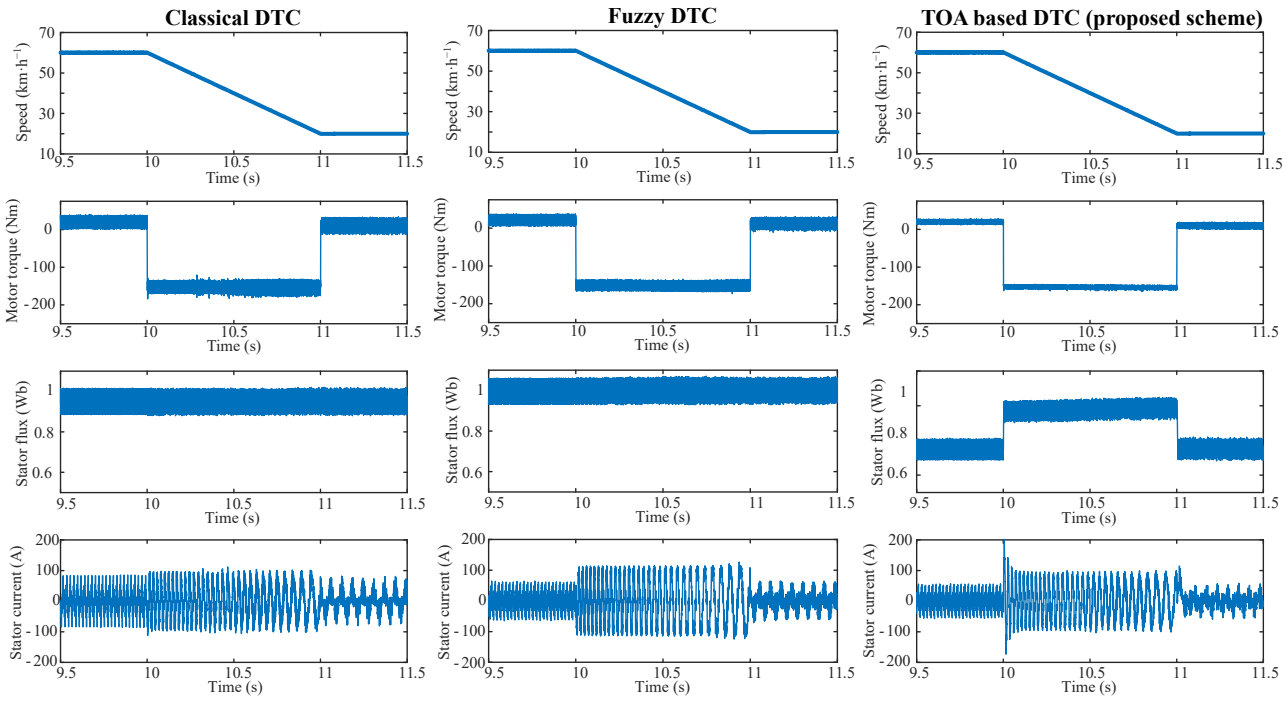

(a) CDTC. (b) FDTC. (c) ODTC.

Fig. 14: Response during braking for (a) CDTC, (b) FDTC, and (c) ODTC methods.

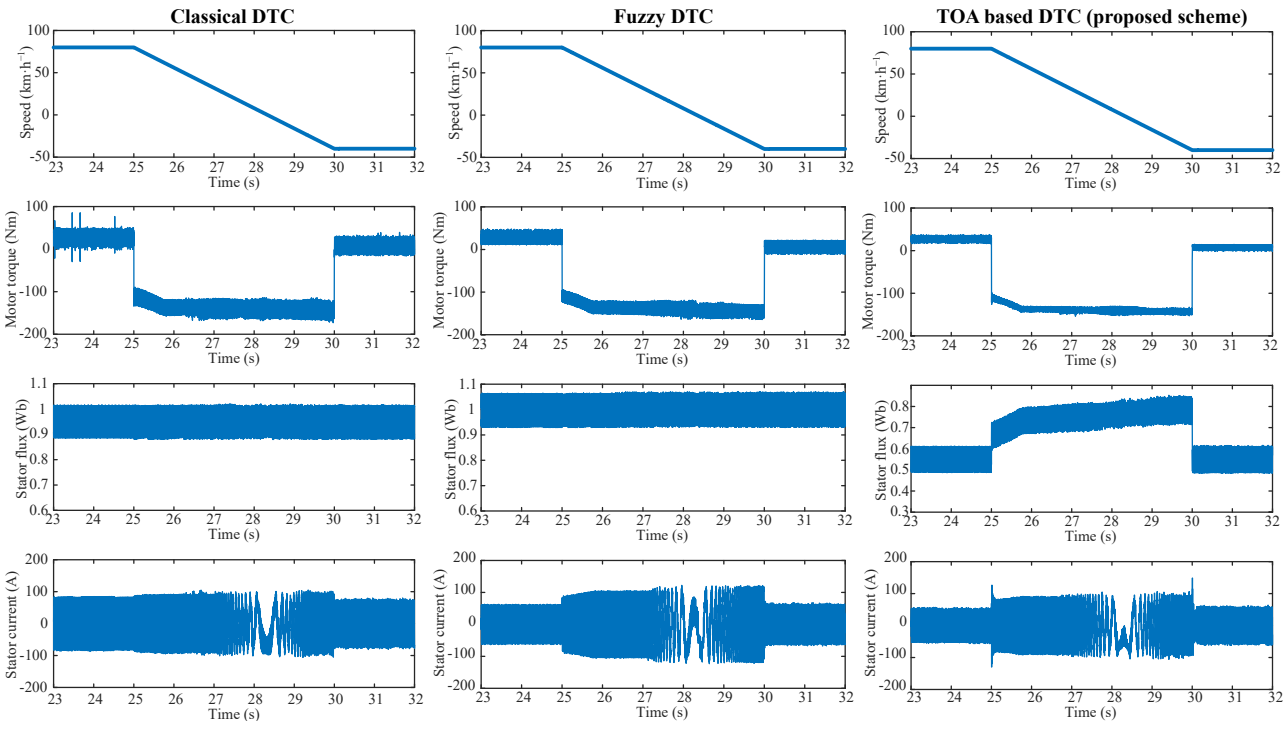

(a) CDTC. (b) FDTC. (c) ODTC.

Fig. 15: Response during speed reversal for (a) CDTC, (b) FDTC, and (c) ODTC methods.

FDTC. As the torque and flux ripple of the proposed DTC is less so, the current magnitude is comparatively small than the other two. Most importantly, the battery energy consumed by the vehicle in both the drive cycles with ODTC is lesser as compared to the other two.

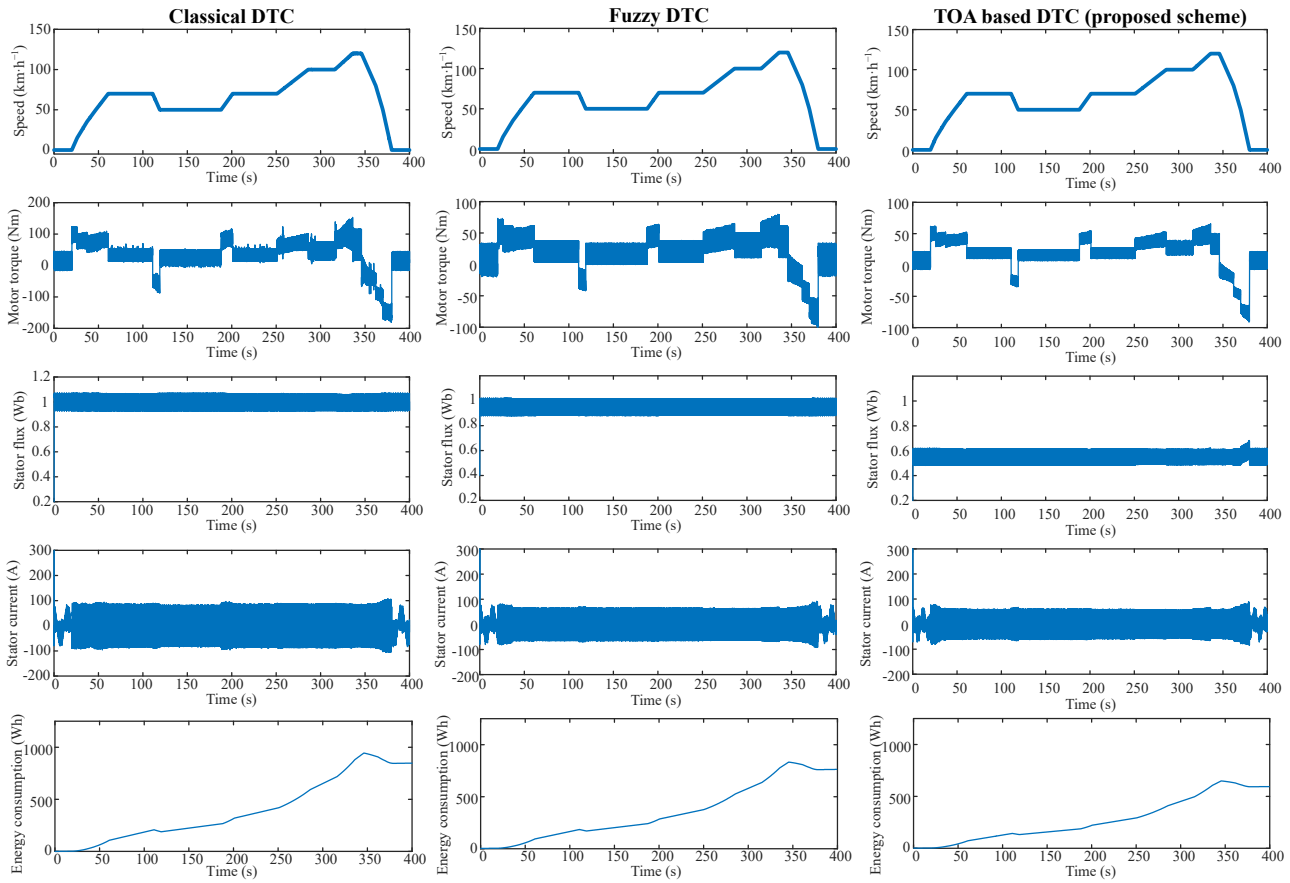

(a) CDTC. (b) FDTC. (c) ODTC.

Fig. 16: Performance of the electric vehicle under EUDC drive cycle with (a) CDTC, (b) FDTC, and (c) ODTC.

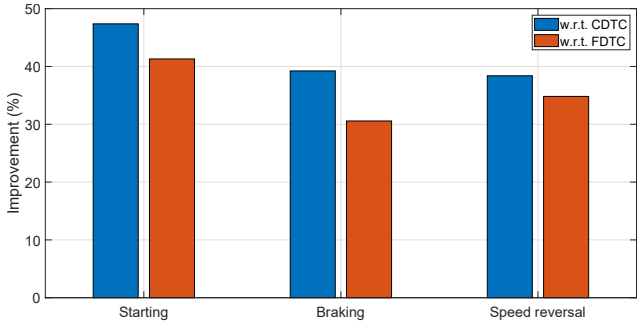

Fig. 17: Improvements in ISE of ODTC during transient.

The energy utilized by the vehicle during the EUDC and HWFET driving cycles is compared in Tab. 5. Figure 19 indicates improvement in the energy consumption by ODTC over the other two approaches. The proposed technique requires less energy than CDTC and FDTC.

Tab. 5: Energy consumption with standard drive cycle.

	CDTC	FDTC	ODTC
EUDC	848.32	629.55	575.17
HWFET	2145.8	1748.3	1185.3

4.4. Performance Index

$$\begin{cases} \text{ISE} = \int_0^T e(t)^2 \mathrm{d}t, \\ \text{ITAE} = \int_0^T t|e(t)|\mathrm{d}t, \\ \text{ITSE} = \int_0^T te(t)^2 \mathrm{d}t. \end{cases} \tag{38}$$

Table 6 compares the performance indices ISE, ITAE, and ITSE for the speed, torque, and flux to determine the superiority of the suggested method over the other two. These are evaluated using the expression as described by Eq. (38), where $e(t)$ is the error in the response.

The performance using these indicators is examined for the drive cycle depicted in Fig. 4 and for the EUDC and HWFET standard drive cycles. The performance indices of the suggested approach is superior to those of the other two for all drive cycles.

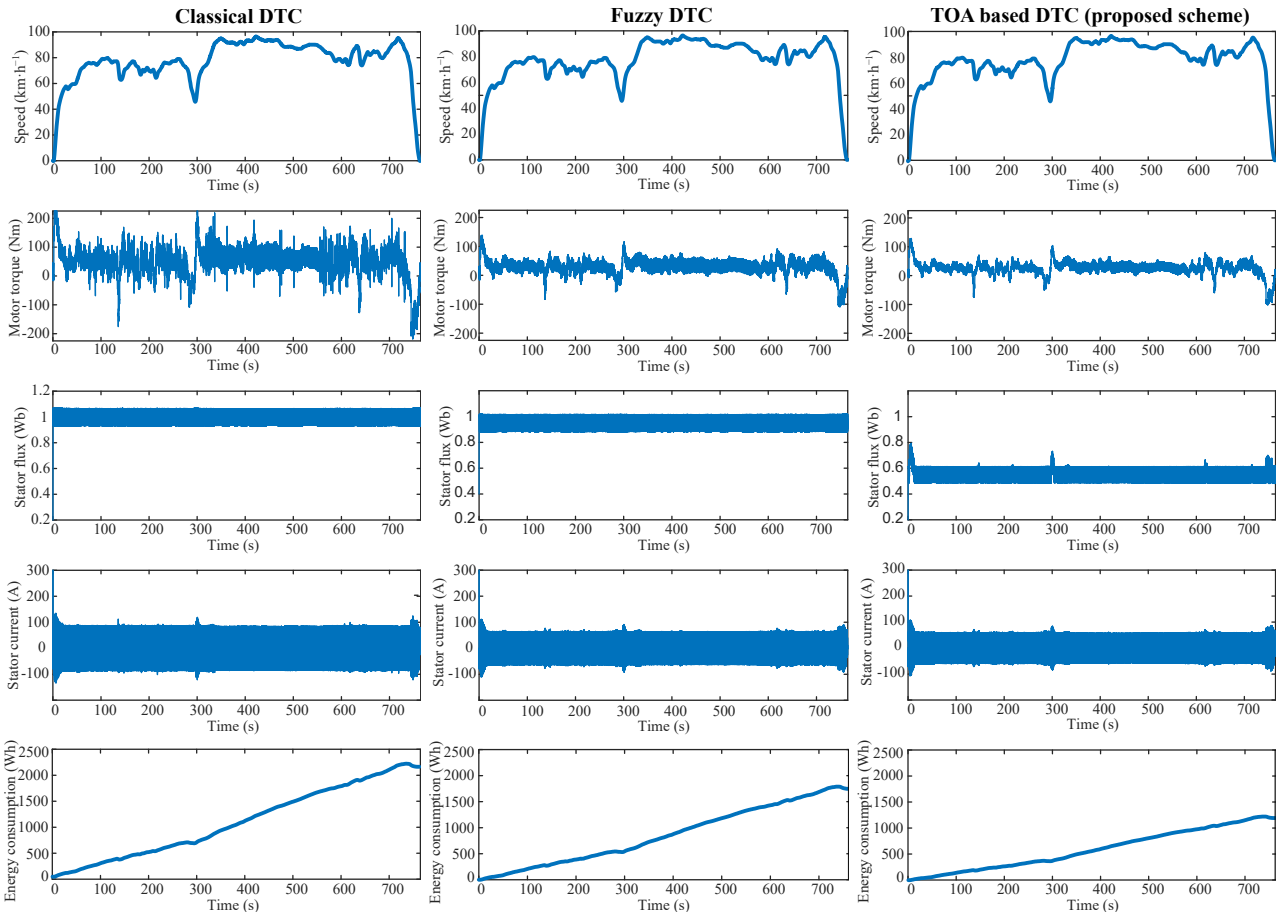

(a) CDTC. (b) FDTC. (c) ODTC.

Fig. 18: Performance of the electric vehicle under HWFET drive cycle with (a) CDTC, (b) FDTC, and (c) ODTC.

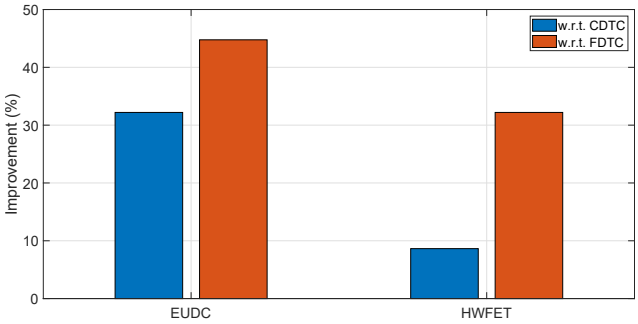

Fig. 19: Improvements in energy consumption of ODTC with standard drive cycle.

4.5. Comparison

Table 7 presents a comparison of the proposed method with approaches published in recent literature. The motor rating can vary depending on the size and weight of the vehicle, and it also differs from the simulated value to the actual motor size utilized for testing. Table 7 presents the performance of motors employed in several published works with varying operating conditions. For the proposed work, a 37 kilowatt IM traveling at 20 km·h^{-1} with a load torque of 119 Nm is considered, and an improvement of 59.32 % and 49.72 %, respectively, is discovered, which is relatively more significant than the other strategies considered.

4.6. Experimental Validation Using OPAL-RT

The suggested strategy is empirically validated in this study by utilizing an OPAL-RT real-time simulator. The OP4510 OPAL-RT is used in this experiment. These devices mimic real-world operations and provide control. Further, the platform for the real-time simulation is equipped with a Xilinx Kintex-7.325T FPGA board with an Intel *Xeon* CPU – 4 cores – 3.5 GHz processor, which is controlled using a host PC. The suggested approach (ODTC) is modeled and simulated in Software-In-the-Loop (SIL) mode utilizing this real-time digital simulator. The fixed time step used for real-time simulation is 25 µs, which is the same as that used in the case of simulation.

Tab. 6: Performance indices.

Drive cycle	Index	Parameters	CDTC	FDTC	ODTC	Improvement (%) w.r.t	
						CDTC	FDTC
Drive cycle as in Fig. 4	ISE	Speed	147.62	126.5498	109.425	25.87	13.53
		Torque	$4.92 \cdot 10^8$	$4.48 \cdot 10^8$	$2.01 \cdot 10^8$	59.06	55.1
		Flux	2048.3447	1934.6351	1426.014	30.38	26.29
	ITAE	Speed	$1.52 \cdot 10^5$	$1.44 \cdot 10^5$	$1.14 \cdot 10^5$	24.84	20.83
		Torque	$5.61 \cdot 10^8$	$5.51 \cdot 10^8$	$3.14 \cdot 10^8$	44	42.92
		Flux	$1.31 \cdot 10^6$	$1.23 \cdot 10^6$	$1.02 \cdot 10^6$	22.59	17.14
	ITSE	Speed	$3.81 \cdot 10^3$	$3.67 \cdot 10^3$	$2.96 \cdot 10^3$	22.4	19.42
		Torque	$1.46 \cdot 10^{10}$	$1.31 \cdot 10^{10}$	$5.95 \cdot 10^9$	59.22	54.48
		Flux	$5.91 \cdot 10^4$	$5.71 \cdot 10^4$	$5.25 \cdot 10^4$	11.25	8.08
HWFET	ISE	Speed	$2.27 \cdot 10^2$	212.4521	103.6128	54.44	51.23
		Torque	$4.82 \cdot 10^9$	$4.67 \cdot 10^9$	$1.53 \cdot 10^9$	68.18	67.15
		Flux	$2.85 \cdot 10^4$	$2.58 \cdot 10^4$	$2.35 \cdot 10^4$	17.45	9.07
	ITAE	Speed	$1.82 \cdot 10^7$	$1.50 \cdot 10^7$	$1.07 \cdot 10^7$	41.14	28.92
		Torque	$8.51 \cdot 10^{10}$	$8.40 \cdot 10^{10}$	$4.88 \cdot 10^{10}$	42.68	41.93
		Flux	$2.58 \cdot 10^8$	$2.10 \cdot 10^8$	$1.87 \cdot 10^8$	27.81	11.05
	ITSE	Speed	$8.01 \cdot 10^4$	$7.86 \cdot 10^4$	$4.08 \cdot 10^4$	49.05	48.06
		Torque	$1.82 \cdot 10^{12}$	$1.79 \cdot 10^{12}$	$6.17 \cdot 10^{11}$	66.15	65.45
		Flux	$1.18 \cdot 10^7$	$1.01 \cdot 10^7$	$8.87 \cdot 10^6$	24.56	12.12
EUDC	ISE	Speed	$1.12 \cdot 10^2$	110.0708	56.5844	49.55	48.59
		Torque	$2.61 \cdot 10^9$	$2.46 \cdot 10^9$	$5.39 \cdot 10^8$	79.35	78.05
		Flux	$1.42 \cdot 10^4$	$1.34 \cdot 10^4$	$1.28 \cdot 10^4$	9.72	4.31
	ITAE	Speed	$4.45 \cdot 10^6$	$4.29 \cdot 10^6$	$2.99 \cdot 10^6$	32.86	30.36
		Torque	$2.51 \cdot 10^{10}$	$2.34 \cdot 10^{10}$	$1.12 \cdot 10^{10}$	55.54	52.33
		Flux	$5.84 \cdot 10^7$	$5.54 \cdot 10^7$	$5.48 \cdot 10^7$	6.1	1.12
	ITSE	Speed	$2.71 \cdot 10^4$	$2.60 \cdot 10^4$	$1.33 \cdot 10^4$	51.08	49.02
		Torque	$5.31 \cdot 10^{11}$	$4.93 \cdot 10^{11}$	$1.18 \cdot 10^{11}$	77.76	76.03
		Flux	$2.82 \cdot 10^6$	$2.63 \cdot 10^6$	$2.58 \cdot 10^6$	8.29	1.63

Tab. 7: Comparison of IM drive for torque ripple control.

Reference	Method	Torque ripple (Nm)	Improvement (%)	Operating Condition
[6]	SVM DTC MBEC SVM DTC	14.8 7.9	46.62	120 W induction motor driven at the rated condition.
[11]	CDTC CSVPWM	6 3.5	41.67	A 5.4 hp motor operated with TL = 27 Nm.
[25]	CDTC FDTC	25.75 14.7	42.91	A 30 kW motor operated with TL = 200 Nm.
[26]	HTFC MST-HTFC	0.61 0.28	54.1	1 kW induction motor drive at the rated condition.
[27]	DTC ODTC		10	1.1 kW IM operated at rated load.
[28]	DTC MTPA-DTC	0.4 0.3	25	
Proposed work	CDTC FDTC ODTC	0.44 0.356 0.179	59.32 49.72	A 37 kW IM is driven at 20 km·h^{-1} with a load torque of 119 Nm.

Figure 21 shows the experimental setup. The performance of the proposed control technique is validated experimentally with the inverter fed 3 hp induction motor, which is mechanically coupled with a DC shunt generator connected with a variable resistive load instead of the speed controller. The DC generator, along with the load box, provides various load torque to the induction motor. Thus, the DTC approach is maximized by decreasing torque ripple while maintaining torque control capabilities across a wide range of operating speeds. To record the experimental results, a Digital Storage Oscilloscope (DSO) is attached to the simulator's output port and another across the motor.

Figure 20 depicts the experimental observations at a low speed of 20 km·h^{-1} for the proposed system and the conventional DTC. The experimental results exhibit a strong correlation with the simulations

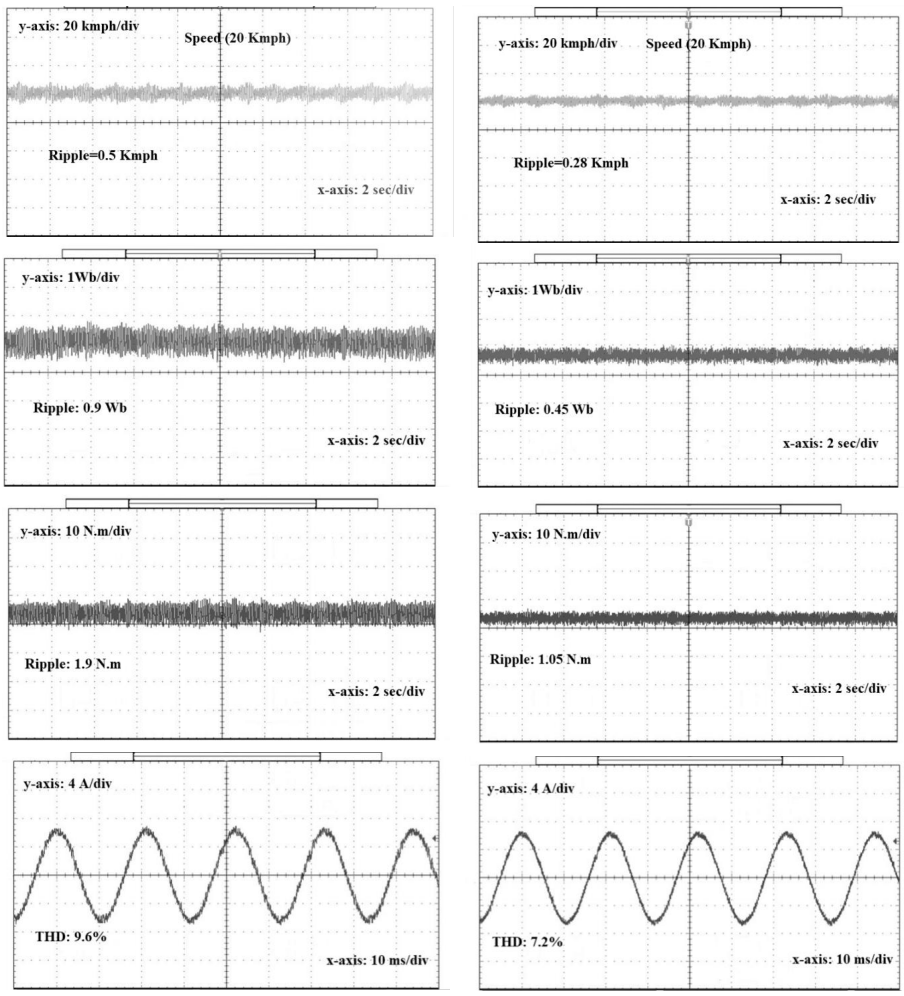

(a) CDTC. (b) ODTC.

Fig. 20: Experimental results at a 20 km·h^{-1} for (a) CDTC (b) ODTC.

Fig. 21: Experimental setup for the proposed method. (A) Host PC, (B) 3-Phase VSI, (C) OpalRt-4510 controller, (D) Induction Motor coupled with DC generator, (E) DSO.

depicted in Fig. 9. The suggested method significantly reduces flux, torque ripples, and harmonics, as demonstrated by the experimental findings.The experimental findings demonstrate a 44.74 % improvement in torque ripple and a 25 % improvement in THD.

5. Conclusion

A TOA-based reference stator flux selection approach was implemented for an IM drive for electric vehicle applications. The primary purpose of this work was to eliminate torque ripple and stator current harmonics. This is accomplished by introducing the appropriate stator flux based on the instantaneous torque, speed, and voltage. To validate this work, a comprehensive simulation analysis of the suggested algorithm is provided, along with a comparison to CDTC and FDTC, over a broad range of speed and driving scenarios. In comparison to the other two techniques,

the suggested algorithm exhibits superior dynamic and steady-state performance with lower torque ripple, stator current THD, flux ripple, and speed error. Additionally, it is estimated that the overall energy consumed by the motor drive for this suggested algorithm is the lowest of all since torque ripple and current THD are reduced. The performance of all three methods was compared with standard drive cycles, and the findings support the efficacy of the proposed technique. The proposed method was experimentally validated using the real-time simulator OPAL-RT 4510 with software in the loop mode.

Author Contributions

R.K.J motivated A.K.S to implement the torque ripple control in electric vehicle applications driven by IM. Beginning with the fundamentals of DTC theory and comparing it to other resilient controllers. R.K.J conceptualized, and provided the methodology. The design and implementation of the research was done by A.K.S., and carried out the simulations of this technique. He wrote the manuscript with the support of R.K.J. The discussion and analysis of the results presented and the writing of the final version of this manuscript was done by both authors.

References

[1] HOU, F., X. CHEN, X. CHEN, F. YANG, Z. MA, S. ZHANG, C. LIU, Y. ZHAO and F. GUO. Comprehensive analysis method of determining global long-term GHG mitigation potential of passenger battery electric vehicles. *Journal of Cleaner Production*. 2021, vol. 289, iss. 1, pp. 1–11. ISSN 1879-1786. DOI: 10.1016/j.jclepro.2020.125137.

[2] TETER, J. Tracking Transport 2020. In: *Policy Commons* [online]. 2020. Available at: `https://policycommons.net/artifacts/1343391/tracking-transport-2020/1955535/`.

[3] XUE, M., B.-L. LIN and K. TSUNEMI. Emission implications of electric vehicles in Japan considering energy structure transition and penetration uncertainty. *Journal of Cleaner Production*. 2021, vol. 280, iss. 1, pp. 1–9. ISSN 1879-1786. DOI: 10.1016/j.jclepro.2020.124402.

[4] EHSANI, M., K. V. SINGH, H. O. BANSAL and R. T. MEHRJARDI. State of the Art and Trends in Electric and Hybrid Electric Vehicles. *Proceedings of the IEEE*. 2021, vol. 109, iss. 6, pp. 967–984. ISSN 1558-2256. DOI: 10.1109/JPROC.2021.3072788.

[5] V, K., R. RAI and B. SINGH. Sliding Model-Based Predictive Torque Control of Induction Motor for Electric Vehicle. *IEEE Transactions on Industry Applications*. 2021, vol. 58, iss. 1, pp. 742–752. ISSN 1939-9367. DOI: 10.1109/TIA.2021.3131973.

[6] SAVARAPU, S., M. QUTUBUDDIN and Y. NARRI. Modified Brain Emotional Controller-Based Ripple Minimization for SVM-DTC of Sensorless Induction Motor Drive. *IEEE Access*. 2022, vol. 10, iss. 1, pp. 40872–40887. ISSN 2169-3536. DOI: 10.1109/ACCESS.2022.3165651.

[7] MALLA, M., S. K. GUDEY and S. SUDHA. Transient and Steady State Characteristics of Induction Motor Drive Using DTC-SVM Technique For EV Applications. In: *2020 11th International Conference on Electrical and Computer Engineering (ICECE)*. Dhaka: IEEE, 2020, pp. 403–406. ISBN 978-1-6654-2254-3. DOI: 10.1109/ICECE51571.2020.9393056.

[8] DE KLERK, M. L. and A. K. SAHA. Performance analysis of DTC-SVM in a complete traction motor control mechanism for a battery electric vehicle. *Heliyon*. 2022, vol. 8, iss. 4, pp. 1–16. ISSN 2405-8440. DOI: 10.1016/j.heliyon.2022.e09265.

[9] EL OUANJLI, N., A. DEROUICH, A. EL GHZIZAL, S. MOTAHHIR, A. CHEBABHI, Y. EL MOURABIT and M. TAOUSSI. Modern improvement techniques of direct torque control for induction motor drives - a review. *Protection and Control of Modern Power Systems*. 2019, vol. 4, iss. 1, pp. 1–12. ISSN 2367-0983. DOI: 10.1186/s41601-019-0125-5.

[10] SAHOO, A. K. and R. K. JENA. Improved DTC strategy with fuzzy logic controller for induction motor driven electric vehicle. *AIMS Electronics and Electrical Engineering*. 2022, vol. 6, iss. 3, pp. 296–316. ISSN 2578-1588. DOI: 10.3934/electreng.2022018.

[11] PATEL, P. D. and S. N. PANDYA. Comparative Analysis of Torque Ripple for Direct Torque Control based Induction Motor Drive with different strategies. *Australian Journal of Electrical and Electronics Engineering*. 2022, vol. 19, iss. 3, pp. 234–252. ISSN 2205-362X. DOI: 10.1080/1448837X.2021.2023249.

[12] ZHANG, Z., H. WEI, W. ZHANG and J. JIANG. Ripple Attenuation for Induction Motor Finite Control Set Model Predictive Torque Control Using Novel Fuzzy Adaptive Techniques. *Processes*. 2021, vol. 9, iss. 4, pp. 1–22. ISSN 2227-9717. DOI: 10.3390/pr9040710.

[13] VAEZI, S. A., H. IMAN-EINI and R. RAZI. A New Space Vector Modulation Technique for Reducing Switching Losses in Induction Motor DTC-SVM Scheme. In: *2019 10th International Power Electronics, Drive Systems and Technologies Conference (PEDSTC)*. Shiraz: IEEE, 2019, pp. 184–188. ISBN 978-1-5386-9254-7. DOI: 10.1109/PEDSTC.2019.8697889.

[14] VO, H. H., M. KUCHAR and P. BRANDSTETTER. Application of fuzzy logic in sensorless induction motor drive with PWM-DTC. *Electrical Engineering*. 2020, vol. 102, iss. 1, pp. 129–140. ISSN 1432-0487. DOI: 10.1007/s00202-019-00810-z.

[15] WANG, G., H. HU, D. DING, N. ZHAO, Y. ZOU and D. XU. Overmodulation Strategy for Electrolytic Capacitorless PMSM Drives: Voltage Distortion Analysis and Boundary Optimization. *IEEE Transactions on Power Electronics*. 2020, vol. 35, iss. 7, pp. 9574–9585. ISSN 1941-0107. DOI: 10.1109/TPEL.2020.2971084.

[16] ZHAO, S., X. HUANG, Y. FANG and H. ZHANG. DC-Link-Fluctuation-Resistant Predictive Torque Control for Railway Traction Permanent Magnet Synchronous Motor in the Six-Step Operation. *IEEE Transactions on Power Electronics*. 2020, vol. 35, iss. 10, pp. 10982–10993. ISSN 1941-0107. DOI: 10.1109/TPEL.2020.2975497.

[17] KABOLI, S., M. R. ZOLGHADRI and E. VAHDATI-KHAJEH. A Fast Flux Search Controller for DTC-Based Induction Motor Drives. *IEEE Transactions on Industrial Electronics*. 2007, vol. 54, iss. 5, pp. 2407–2416. ISSN 1557-9948. DOI: 10.1109/TIE.2007.900341.

[18] SUBRAMANIAM, S. K., J. X. RAYAPPAN and B. SUKUMAR. Fuzzy-based estimation of reference flux, reference torque and sector rotation for performance improvement of DTC-IM drive. *Automatika*. 2022, vol. 63, iss. 3, pp. 440–453. ISSN 1848-3380. DOI: 10.1080/00051144.2022.2051966.

[19] KUMAR, S. S., R. J. XAVIER and S. BALAMURUGAN. Development of ANFIS-based reference flux estimator and FGS-tuned speed controller for DTC of induction motor. *Automatika*. 2018, vol. 59, iss. 1, pp. 11–23. ISSN 1848-3380. DOI: 10.1080/00051144.2018.1486796.

[20] SAHOO, A. K. and R. K. JENA. Loss minimisation of induction motor-driven electric vehicle using teamwork optimisation. *International Journal of Ambient Energy*. 2022, vol. 43, iss. 1, pp. 8123–8134. ISSN 2162-8246. DOI: 10.1080/01430750.2022.2091036.

[21] TAKAHASHI, I. and T. NOGUCHI. A New Quick-Response and High-Efficiency Control Strategy of an Induction Motor. *IEEE Transactions on Industry Applications*. 1986, vol. 22, iss. 5, pp. 820–827. ISSN 1939-9367. DOI: 10.1109/TIA.1986.4504799.

[22] DEPENBROCK, M. Direct self-control (DSC) of inverter fed induktion machine. In: *1987 IEEE Power Electronics Specialists Conference*. Blacksburg: IEEE, 1987, pp. 632–641. DOI: 10.1109/PESC.1987.7077236.

[23] MANIAS, S. *Power Electronics and Motor Drive System*. 1st ed. London: Academic Press, 2016. ISBN 978-0-12-811798-9.

[24] DEHGHANI, M. and P. TROJOVSKY. Teamwork Optimization Algorithm: A New Optimization Approach for Function Minimization/Maximization. *Sensors*. 2021, vol. 21, iss. 13, pp. 1–26. ISSN 1424-8220. DOI: 10.3390/s21134567.

[25] MAITY, P. and A. VIJAYAKUMARI. Fuzzy-Enabled Direct Torque Control for Low Torque Ripple in Induction Motors for EV Applications. In: *International Conference on Emerging Trends and Advances in Electrical Engineering and Renewable Energy*. Bhubaneswar: Springer, 2020, pp. 371–383. ISBN 978-981-15-7511-2. DOI: 10.1007/978-981-15-7511-2_35.

[26] RAVI, H. K. and L. N. CHOKKALINGAM. Current ripple reduction to improve electromagnetic torque and flux characteristics in AC drives. *International Journal of Electronics*. 2022, vol. 109, iss. 8, pp. 1421–1442. ISSN 1362-3060. DOI: 10.1080/00207217.2021.1969443.

[27] TARUSAN, S. A. A., A. JIDIN and M. L. M. JAMIL. The optimization of torque ripple reduction by using DTC-multilevel inverter. *ISA Transactions*. 2022, vol. 121, iss. 1, pp. 365–379. ISSN 1879-2022. DOI: 10.1016/j.isatra.2021.04.005.

[28] NAGANATHAN, P. and S. SRINIVAS. MTPA Associated DTC Methodologies for Enhanced Performance and Energy Savings in Electric Vehicle Mobility With Induction Motor Drive. *IEEE Transactions on Transportation Electrification*. 2021, vol. 8, iss. 2, pp. 1853–1862. ISSN 2332-7782. DOI: 10.1109/TTE.2021.3130178.

About Authors

Anjan Kumar SAHOO (corresponding author) was born in Odisha, India. He received his B.Tech.

degree in Electrical Engineering from the Biju Patnaik University of Technology (BPUT), Rourkela, India in 2009; and his M.Tech. degree in Electrical Engineering from Indian Institute of Technology, Kharagpur, India in 2013. He is presently working towards his Ph.D. degree in BPUT, Rourkela, India. He is currently an Assistant Professor in the Department of Electrical Engineering, Odisha University of Technology and Research, Bhubaneswar, Odisha, India. His research interests include electrical machines, drives, and electric vehicles.

Ranjan Kumar JENA was born in Odisha, India. He received his M.E. degree in Electronics Systems and Communication Engineering from Regional Engineering College, Rourkela, India in 1996; and his Ph.D. degree from Sambalpur University, India in 2005. He has teaching experience of more than 20 years in engineering colleges. He is presently working as a professor in the Department of Electrical Engineering, Centre for Advanced Post Graduate Studies, Biju Patnaik University of Technology, Rourkela, India. He has more than 30 research publications. His research interests include power electronics control, and design, electric vehicles, energy conversion, and renewable energies.